Supplementary Information (SI) for Journal of Materials Chemistry A.
This journal is © The Royal Society of Chemistry 2026

Supporting Information

MFU-4 as a Benchmark Molecular Sieve for Efficient CO_2/CH_4 Separation in Biogas Upgrading

Adriano Henrique[a], Prantar Dutta[b,c], Mayank Gupta[d], Georges Mouchaham[d*], Yann Magnin[c], Christian Serre[d], Guillaume Maurin[b,e*] and José A. C. Silva[a*]

[a] Centro de Investigação de Montanha (CIMO), Instituto Politécnico de Bragança, Campus Santa Apolónia, 5300-253 Bragança, Portugal

[b] ICGM, Univ. Montpellier, CNRS, ENSCM, Montpellier, France

[c] OneTech, R&D, CSTJF, TotalEnergies, Pau 64018, France

[d] Institut des Matériaux Poreux de Paris, ESPCI Paris, Ecole Normale Supérieure, CNRS, PSL University, Paris 75005, France

[e] Institut Universitaire de France, France

[*] Corresponding Authors: Georges Mouchaham (georges.mouchaham@ens.psl.eu), Guillaume Maurin (guillaume.maurin1@umontpellier.fr), José A. C. Silva (jsilva@ipb.pt)

List of Symbols

Nomenclature

b	adsorption affinity constant of component i, (kPa^{-1})
b_∞	adsorption affinity constant of component i at infinite temperature, (kPa^{-1})
c_i	concentration of component i, ($mol \cdot m^{-3}$)
d_s	diameter of the adsorbent, (m)
$D_{ax,i}$	axial mass dispersion coefficient of component i, ($m^2 \cdot s^{-1}$)
D_i	micropore diffusivity of component i, ($m^2 \cdot s^{-1}$)
D_{ij}	binary diffusivity for the pair of components i and j, ($m^2 \cdot s^{-1}$)
$D_{m,i}$	molecular diffusion coefficient of component i, ($m^2 \cdot s^{-1}$)
E_i	activation energy for diffusion of component i, ($J \cdot mol^{-1}$)
F	molar flux of component i, ($mol \cdot m^2 \cdot s^{-1}$)
F_f	molar flux of component i in the feed, ($mol \cdot m^2 \cdot s^{-1}$)
ΔH_i	heat of adsorption of component i, ($J \cdot mol^{-1}$)
$k_{LDF,i}$	mass transfer coefficient of component i, (s^{-1})
$k_{LDF\infty,i}$	mass transfer coefficient of component i at infinite temperature, ($kPa \cdot s^{-1}$)
m_s	mass of adsorbent, (kg)
M_i, M_j	Molar mass of component i and j, respectively, ($kg \cdot mol^{-1}$)
M_g	average molar mass of the gas mixture, ($kg \cdot mol^{-1}$)
N	number of components in the gas mixture, (-)
P	total pressure, (kPa)
p	partial pressure of component i in the gas mixture, (kPa)
Q_{st}	isosteric heat of adsorption, ($J \cdot mol^{-1}$)
q_{exp}	loading of component i (experimental), ($mol \cdot kg^{-1}$)
q_i	loading of component i (given by the isotherm model = q_{model}), ($mol \cdot kg^{-1}$)
$\bar{q}_i$	averaged loading of component i, ($mol \cdot kg^{-1}$)
$q_{sat,i}$	saturation loading capacity of component i, ($mol \cdot kg^{-1}$)
R	universal gas constant, ($J \cdot mol^{-1} \cdot K^{-1}$)
r_c	crystal (microparticle) radius, (m)
r_s	radius of adsorbent particles, (m)

S_{CO_2/CH_4}	selectivity of CO_2 relative to CH_4, (-)
t	time, (s)
t_{sat}	saturation time, (s)
T^*	dimensionless temperature in the diffusion collision integral, (-)
T_g	temperature of the bulk gas phase, (K)
T_s	temperature of the solid phase, (K)
v_g	superficial velocity of the gas mixture, ($m \cdot s^{-1}$)
v_{int}	interstitial velocity of the gas mixture, ($m \cdot s^{-1}$)
WC	working capacity, ($mol \cdot kg^{-1}$)
y_i	molar fraction of component i, (-)
z	distance along the length of the adsorption column (axial coordinate), (m)

Greek Letters

ε_b	interparticle voidage, ($m^3_{void} \cdot m^3_{bed}$)
ε_t	total bed voidage, ($m^3_{void+pore} \cdot m^3_{bed}$)
ε_i, ε_j	maximum energy of attraction for the components i or j, respectively, (J)
ε_{ij}	maximum energy of attraction for the pair of components i and j, (J)
κ	Boltzmann constant, ($J \cdot K^{-1}$)
μ_g	viscosity of the gas mixture, (kPa·s)
ρ_b	adsorbent bulk density, ($kg \cdot m^{-3}$)
ρ_g	density of the gas mixture, ($kg \cdot m^{-3}$)
σ_i, σ_j	collision diameter for the components i and j, respectively, (Å)
$\sigma_{i,j}$	collision diameter for the pair of components i and j, (Å)
$\Omega_{D_{ij}}$	collision integral for diffusion for the pair of components i and j, (-)
ψ	adsorbent shape factor, (-)

Subscripts

ax	axial
c	crystal
f	feed
g	gas mixture

i, j	i or j component in the gas mixture
int	interstitial
s	solid (adsorbent particle)
∞	infinite condition

S1. Methodology

S1.1 Characterization of MFU-4(Zn)

IR spectra were collected at ambient condition on a Nicolet iS5 FTIR ThermoFisher spectrometer. Powder X-ray diffraction (PXRD) data were collected at ambient temperature using a high-throughput Bruker D8 Advance diffractometer operating in transmission mode, equipped with a focusing Göbel mirror (CuKα radiation, λ = 1.5418 Å) and a LynxEye detector. N_2 adsorption isotherms at 77 K were measured on a Micromeritics Tristar instrument, while CO_2 adsorption isotherms at 298 K were recorded using a Micromeritics TriFlex apparatus. All adsorption measurements were carried out with ultra-high purity gases (≥ 4.8 grade). Prior to analysis, samples were degassed at 250 °C for 12 h using a Micromeritics SmartVacPrep unit, and complete activation was confirmed by an outgassing rate ≤ 2 μbar·min^{-1}. Scanning electron microscopy (SEM) coupled with energy-dispersive X-ray spectroscopy (EDX) was performed using a FEI Magellan 400 microscope. Thermogravimetric analysis (TGA) was conducted on a Mettler Toledo TGA/DSC 2 (STAR System) instrument with a heating rate of 5 °C·min^{-1} under flowing oxygen. Fourier-transform infrared (FTIR) spectra were recorded on a Thermo Scientific Nicolet iS5 spectrometer.

S.1.1.1 FT-IR spectroscopy

The FT-IR spectrum of the non-activated pristine MFU-4 confirms the successful formation of the Zn–bistriazolate framework and the presence of residual guest molecules inside the pores. A broad band centered at ~3438 cm^{-1} is attributed to O–H stretching of adsorbed moisture. Weak absorptions around ~3080 cm^{-1} correspond to aromatic C–H stretching of the organic linker, while bands at ~2918 and ~2848 cm^{-1} arise from aliphatic C–H stretching vibrations of occluded solvent molecules. A strong band observed at ~1652 cm^{-1} is assigned to the C=O stretching vibration of DMF, indicating the retention of guest solvent within the framework. The fingerprint region displays characteristic bands at ~1487, 1434, 1408 and 1381 cm^{-1}, which originate from ring stretching vibrations of the triazolate/aromatic moieties and C–N related modes of the linker. Additional intense bands at ~1310 and ~1200 cm^{-1} (strong), together with absorptions at ~1163, 1092 and 1056 cm^{-1}, further support the presence of bistriazolate ligand vibrations. The band at ~862 cm^{-1} corresponds to aromatic C–H out-of-plane bending. Low-wavenumber features below 700 cm^{-1} (e.g., ~659, 569, 469 and 425 cm^{-1}) are attributed to framework lattice vibrations including Zn–N/Zn–Cl stretching modes, consistent with the formation of MFU-4 (Figure S1).

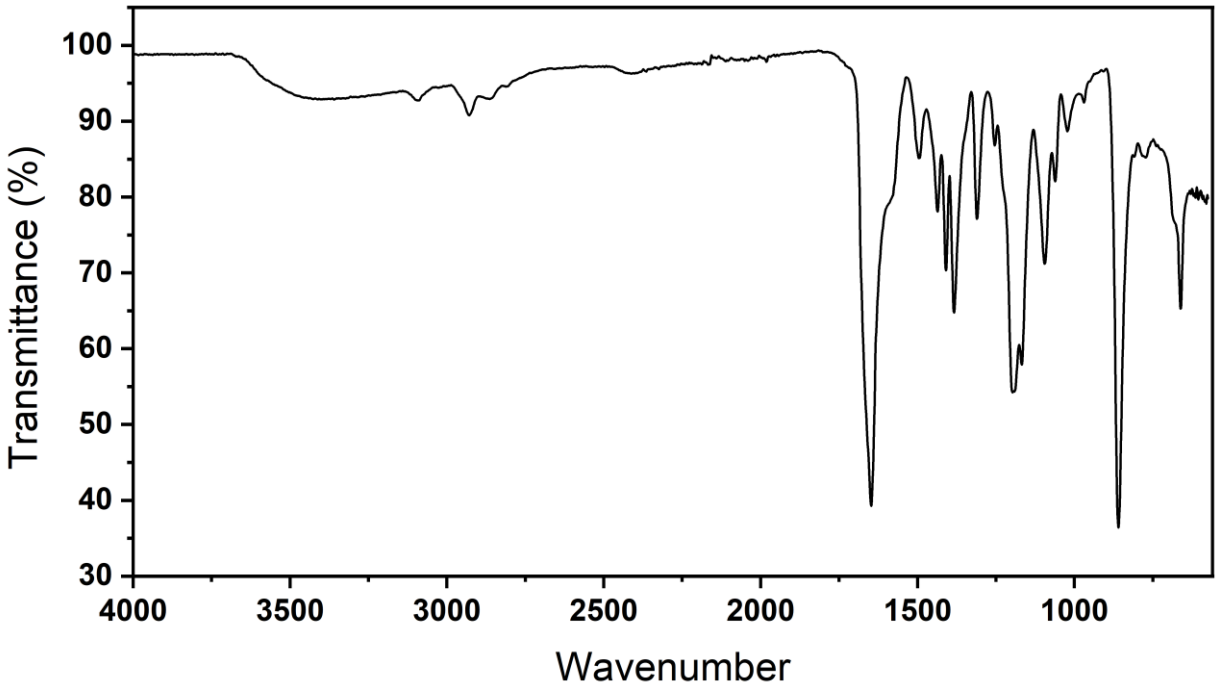

Figure S1. FT-IR spectra of the pristine non-activated MFU-4 sample.

S.1.1.2 Powder x-ray diffraction

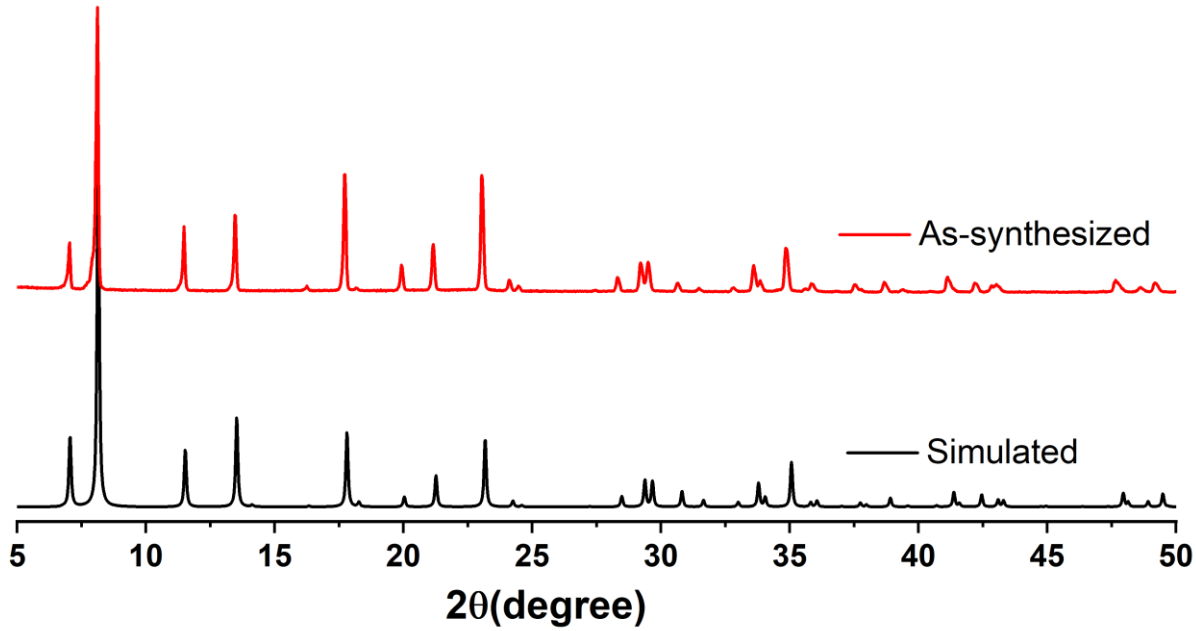

Figure S2. PXRD patterns of as-synthesized MFU-4 and the simulated pattern derived from the reported crystal structure Cu Kα (λ = 1.5418 Å).

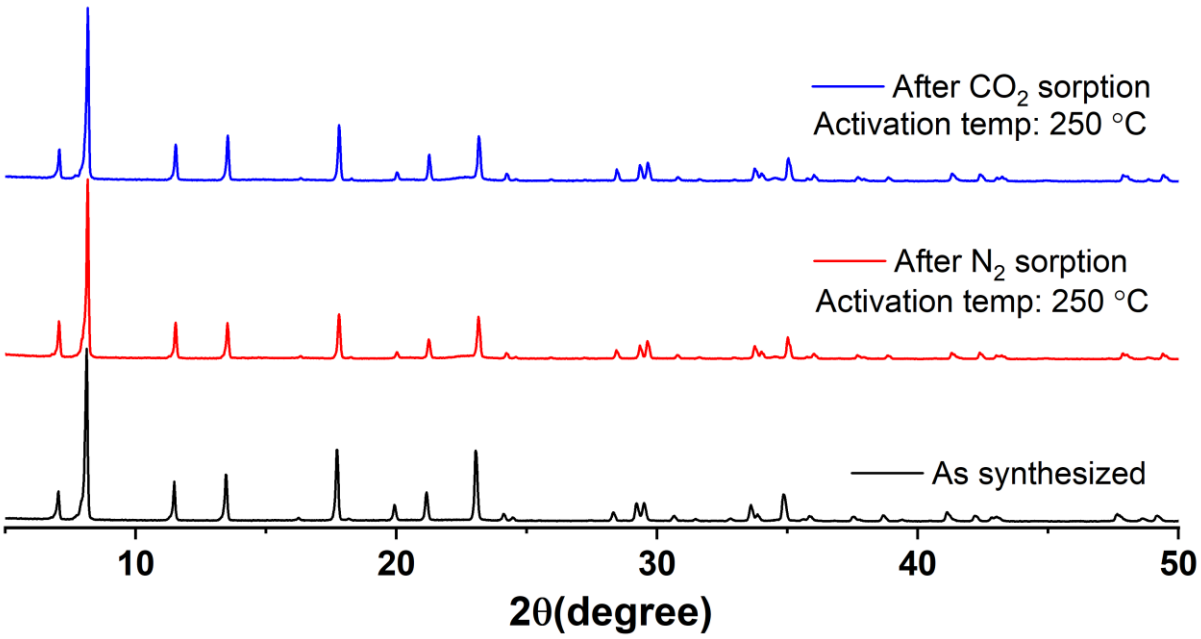

Figure S3. PXRD patterns of MFU-4 in the as-synthesized state and after activation at 250 °C followed by CO_2 and N_2 sorption, demonstrating retention of crystallinity Cu Kα (λ = 1.5418 Å).

S.1.1.3 Scanning electron microscopy and energy dispersive x-ray analysis

The scanning electron microscopy (SEM) images of the as-synthesized MFU-4 confirm the formation of highly crystalline microcrystalline particles with well-developed facets. The product predominantly consists of blocky/cubic-shaped crystals with sharp edges and smooth faces, together with a noticeable fraction of octahedral-like crystallites, indicating the coexistence of multiple growth habits for the MFU-4 framework under solvothermal synthesis conditions. The crystals are fairly uniform in shape; however, a moderate size dispersion is evident. From the SEM scale bars, the particle size is in the micrometer range (≈ 0.5–5 µm), with most crystals typically falling around ~1–3 µm. In addition, mild particle clustering/agglomeration is observed, which is commonly attributed to drying/solvent removal and interparticle adhesion in MOF powders. Overall, the observed morphology (mixed cubic and octahedral crystals with well-defined facets) is consistent with the characteristic SEM features reported for MFU-4 in literature, confirming successful framework formation (Figure S4).

Energy-dispersive X-ray (EDX) analysis was performed to examine the inorganic composition of MFU-4. The framework has the chemical formula $[Zn_5Cl_4(BBTA)_3]\cdot 3DMF$, corresponding to a theoretical Zn:Cl atomic ratio of 1:0.80. Based on the averaged EDX atomic percentages (Zn = 52.53 at %, Cl = 47.47 at.%), the experimental Zn:Cl ratio is approximately 1:0.85 and 1.09 for cubic and octahedral shaped crystals. Nevertheless, the experimental ratio is in good agreement with the proposed MFU-4 stoichiometry and confirms the formation of the

Zn–Cl-based inorganic nodes characteristic of MFU-4. No additional inorganic elements were detected, indicating high chemical purity of the synthesized material.

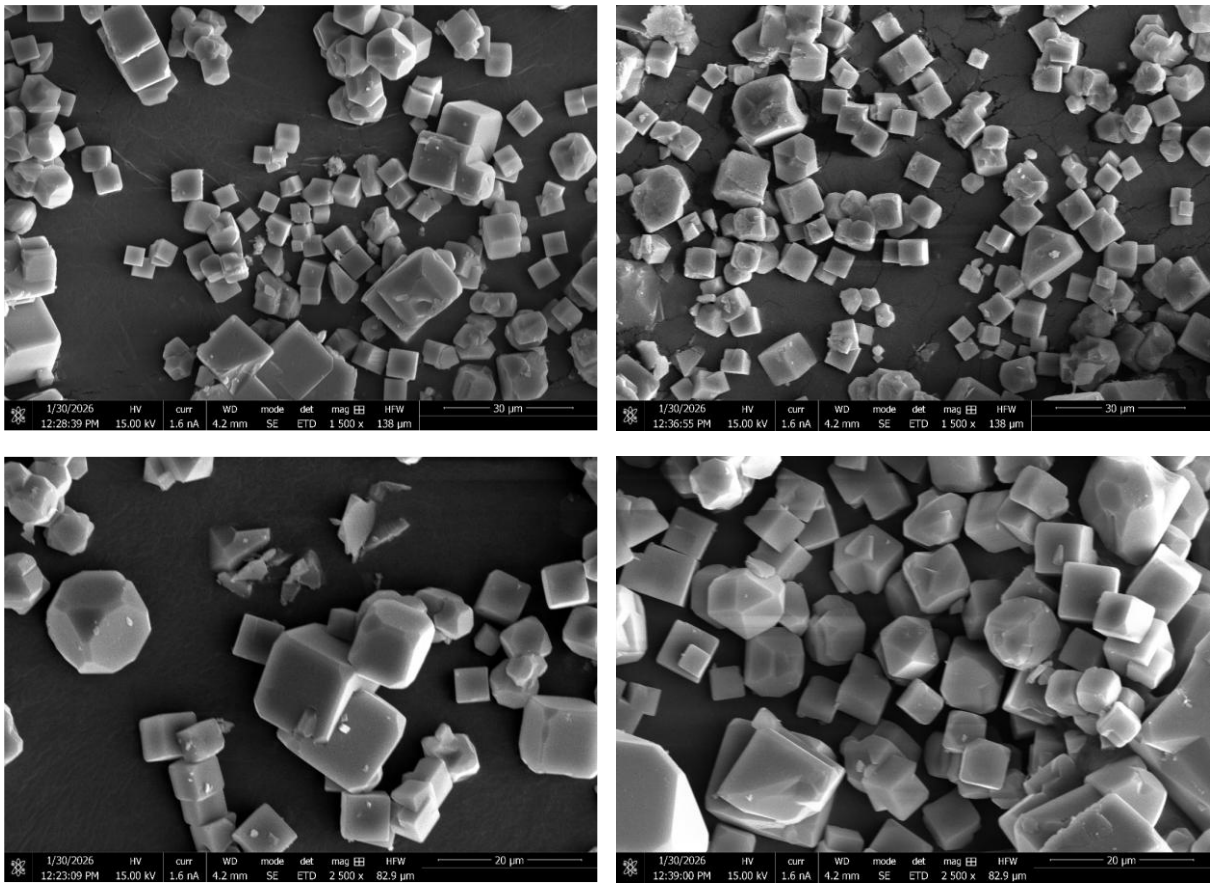

Figure S4. SEM image of compound MFU-4.

S.1.1.4 Thermogravimetric analysis

Thermogravimetric analysis (TGA) was performed to evaluate the purity, thermal behavior, and guest (DMF) content of MFU-4 in its as-synthesized form. Literature reports for MFU-4·DMF describe an initial mass loss of ~18 wt% in the range of 120–250 °C, corresponding to the release of approximately three trapped DMF molecules per formula unit, confirming that the framework is obtained in a solvated state after synthesis. In our case, the TGA profile also exhibits a multistep weight-loss behavior (Figure S5). An initial mass loss of ~9 wt% between 25 and 80 °C is attributed to the removal of surface-adsorbed moisture and residual lattice water. This experimental value closely matches the theoretical water content of 8.47 wt% calculated for six water molecules per formula unit. The subsequent mass loss of ~18 wt% observed between 120 and 300 °C is assigned to the release of entrapped DMF molecules and agrees well with the theoretical DMF content of 17.18 wt% for three DMF molecules. At higher temperatures (above ~420 °C), a sharp mass drop of ~49 wt% is observed, corresponding to framework decomposition; this is in very good agreement with the calculated combined ligand

and chlorine contribution of 48.75 wt%. The close parallel between experimental and theoretical values supports the formulation $[Zn_5Cl_4(BBTA)_3]\cdot 3DMF\cdot 6H_2O$ rather than the simplified $[Zn_5Cl_4(BBTA)_3]\cdot 3DMF$ model. Upon complete thermal degradation under oxidative conditions, the framework ultimately decomposes to form ZnO as the final inorganic residue. After activation at 250 °C, the TGA curves measured for MFU-4 after CO_2 and N_2 gas sorption measurements become significantly different from the as-synthesized samples. In both activated materials, the characteristic solvent-loss contribution is largely absent, confirming that activation at 250 °C effectively removes pore-confined DMF and yields the desolvated MFU-4 framework. Notably, both activated samples show 24% mass loss at low temperature (typically below ~100 °C), which is attributed to readsorbed water/moisture uptake upon exposure to air after activation, rather than solvent loss or framework degradation. This assignment is further supported by the literature activation/air-exposure TGA data,[1] where an activated MFU-4 sample exposed to air exhibits an early mass decrease and retains ~76 wt% at 100 °C, consistent with desorption of physically adsorbed water at low temperature. Importantly, the activated MFU-4 samples (after CO_2 and N_2 sorption) remain thermally stable up to the onset of decomposition at higher temperatures, where a sharp weight-loss step occurs due to framework breakdown, ultimately yielding comparable residual masses (Figure S6).[1]

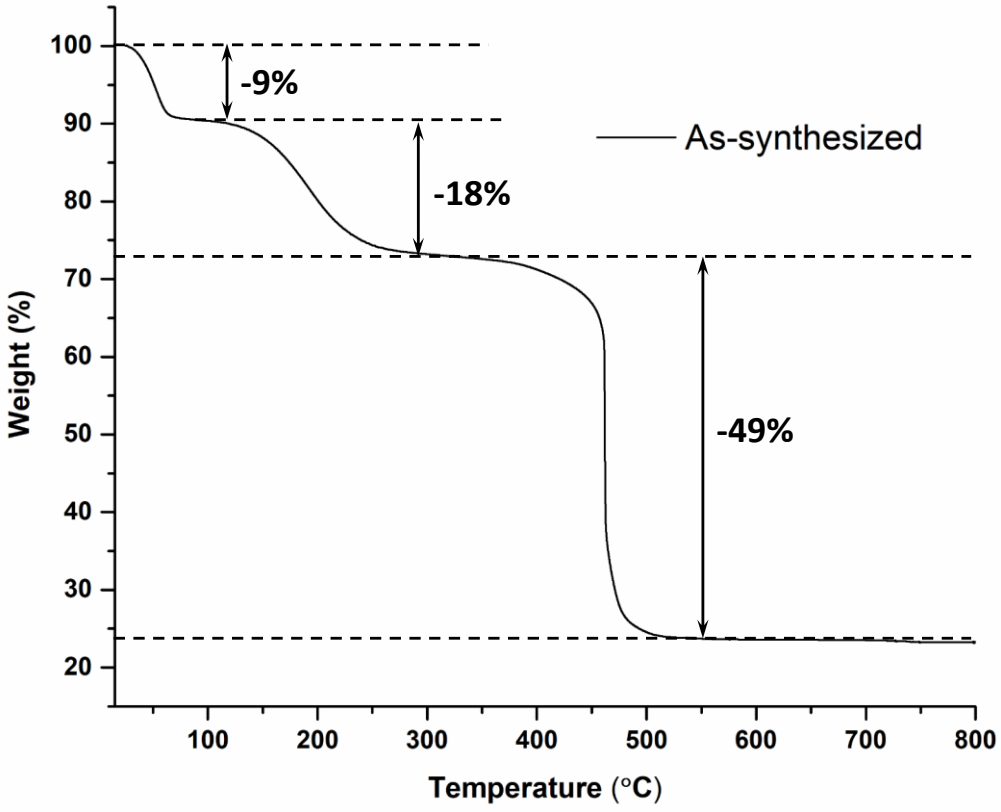

Figure S5. Thermogravimetric analysis of MFU-4 with a heating rate of 5 °C·min^{-1} under oxygen flow.

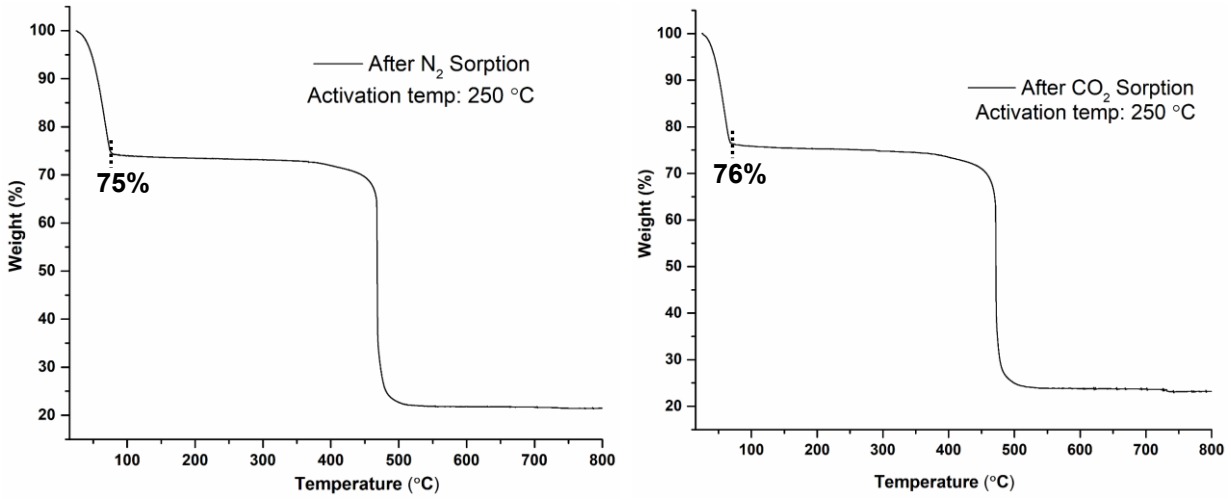

Figure S6. TGA curves of MFU-4 after activation at 250 °C, recorded after N_2 (left) and CO_2 (right) sorption.

S1.2 Fixed Bed Adsorption: Experimental and Numerical Simulation

S1.2.1 Experimental apparatus

The fixed-bed adsorption apparatus used to measure single- and multicomponent breakthrough curves is shown in Figure S7. In the gas preparation section, the partial pressure of pure CO_2 or CO_2/CH_4 feed mixtures are set before being introduced into the adsorption column. Four mass flow controllers (MFC1–4; Bronkhorst High-Tech B.V.) regulate the flow rates, and two back-pressure controllers (BPC1–2; Bronkhorst High-Tech B.V.) maintain the total system pressure. Before each experiment, the pure gas or mixture flows through line 1 to an automatic four-port valve (aV1; VICI, Valco Instruments Co.), pressurized by BPC1. Simultaneously, pure He, used as the carrier gas, flows through line 2 (adsorption column) and line 3 (makeup line to accelerate the outlet stream). Both lines are controlled by BPC2. The adsorption column (316 stainless steel, CS-Chromatographie-Service GmbH) is 0.033 m long, with an internal diameter of 0.0046 m, and is immersed in a temperature-controlled water bath (Witeg) equipped with a circulation pump to ensure temperature uniformity.

To adjust partial pressure of CO_2 in a combination with He for single component experiments, on-off ball valves (bV1–bV2; 316 stainless steel, Swagelok) were closed and opened, respectively. Once all operating conditions (temperature, pressure, and flowrates) are set, the experiment begins by switching aV1, allowing the adsorbate to enter the column. The outlet stream is directed to a gas chromatograph (GC, Agilent Technologies) and continuously monitored by the TCD detector via line 4. For the multicomponent studies, the outlet stream first passes through an automatic six-port sampling valve (aV2; VICI, Valco Instruments Co.) with a 5 µL loop. The valve operates cyclically, injecting aliquots carried by He into a GC packed

column (316 stainless steel, length 3 m x OD 1/8" x ID 2 mm, packed with Hayesep D, 80/100 mesh), for peak separation prior to TCD analysis. For this operation, the 3-way ball valve (bV3; 316 stainless steel, Swagelok) is switched.

Chromatographic analyses were performed under the following conditions: oven temperature, 313 K; TCD temperature, 423 K, with a reference flowrate of 20 $mL \cdot min^{-1}$; packed column temperature, 423 K, with a He flowrate of 50 $mL \cdot min^{-1}$. The sampling valve operated in 20 s cycles, with 10 s in the load position and 10 s in the inject position. To confirm MFC stabilization, a manual bubble flowmeter (Supelco) was used to verify each MFC's set-point flowrate. The gases were supplied by Air Liquide with the following purities: He 5.0 (99.999%), CO_2 N48 (99.998%), and CH_4 N35 (99.95%).

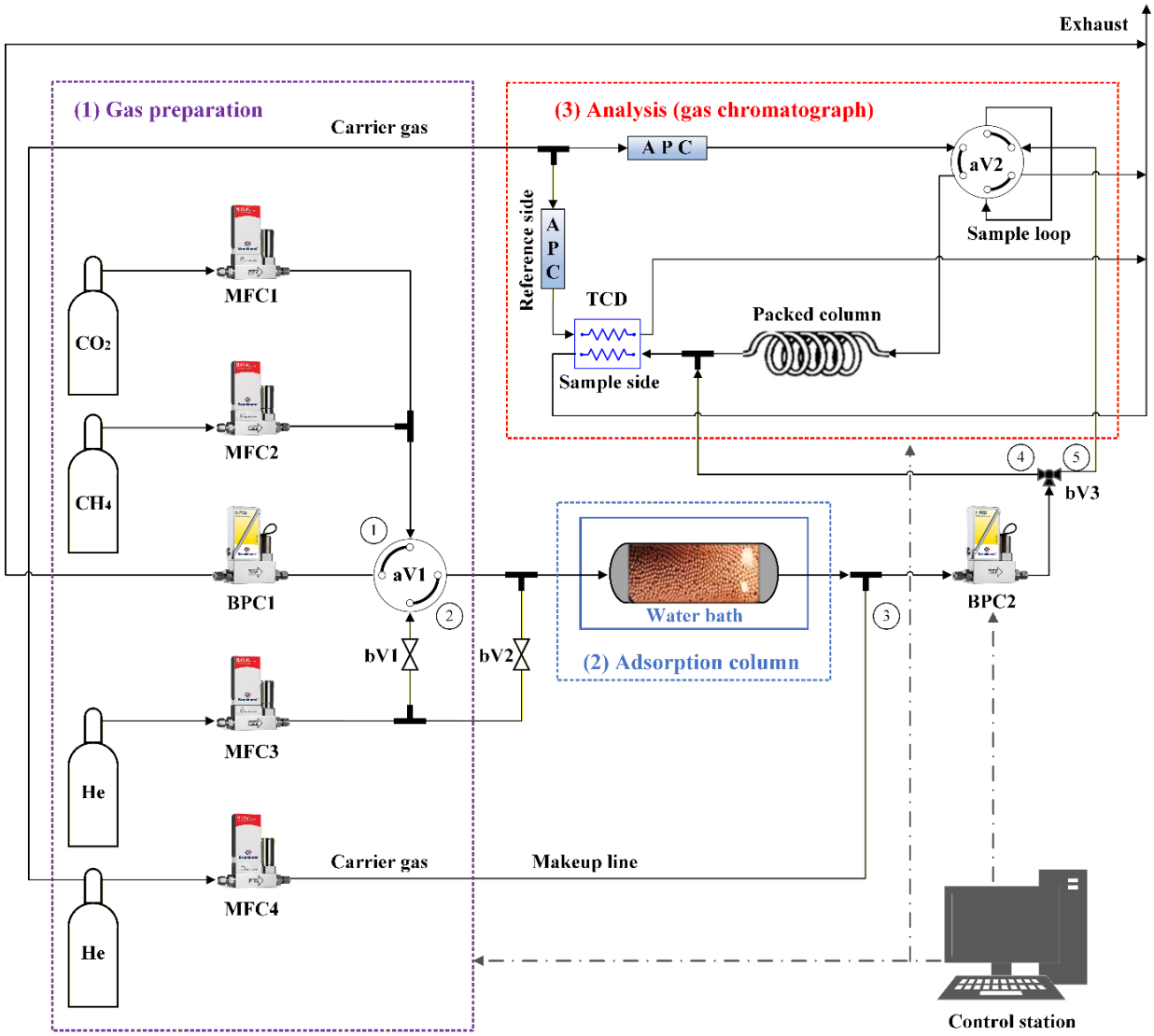

Figure S7. Schematic diagram of the fixed-bed adsorption apparatus for measuring single (CO_2) and binary (CO_2/CH_4) breakthrough curves. MFCs: mass flow controller; BPC back pressure controller; aV: automatic valve; bV: ball valves; APC advanced pneumatic control; TCD: thermal conductivity detector; GC packed column: Hayesep D.

S.1.2.2 Adsorbent preparation

Prior to the adsorption experiments, the MFU-4 powder was shaped into small agglomerates to avoid pressure drop following a procedure described elsewhere.[2] First, the powder was compacted into disks using a manual hydraulic press (*Atlas® 15T, Specac*) at 6.5 kg·mm^{-2} for 5 min. The disks were then broken into fragments of approximately 2 mm. To remove any pre-adsorbed moisture from synthesis and handling, the material was degassed in a muffle furnace (ThermConcept) at 423 K under vacuum with a He flow of 5 mL·min^{-1} for 12 h.

S.1.2.3 Adsorption loading

All experimental runs were compared with blank experiments using a column packed with glass spheres under identical operating conditions to determine the dead volume of the system. This value was subsequently used to correct the calculated adsorption equilibrium loadings, which were obtained by integrating the molar flow profiles of the corrected breakthrough curves according to the following equation:

$$q_{exp} = \frac{1}{m_s}\left(F_f t_{sat} - \int_0^{t_{sat}} F dt\right) \tag{S1}$$

S.1.2.4 Fitting of pure component isotherms

The pure component adsorption equilibrium data of CO_2 (obtained from experimental breakthrough curves) and CH_4 (determined from GCMC simulations) were fitted using the Dual-Site Langmuir model for CO_2 and the single-site Langmuir model for CH_4,[3] as follows:

$$q_i = \sum_{i=1}^{N} q_{sat_i} \frac{(b_i p)}{1 + (b_i p)} \tag{S2}$$

with the temperature dependence of the affinity constant b_i described by the Arrhenius expression:

$$b_i = b_{\infty,i}\, exp\left(\frac{-\Delta H_i}{R T_s}\right) \tag{S2.1}$$

S.1.2.5 Isosteric Heat of Adsorption

The isosteric heat of adsorption, Q_{st}, was determined with the Clausius-Clapeyron equation.[4,5] This relationship, in its differential form at constant coverage, is given by:

$$Q_{st} = RT^2 \left(\frac{\partial \ln p}{\partial T_s}\right)_q \quad \text{(S3)}$$

The Q_{st} values were then calculated by linear regression, plotting $ln\, p$ against $1/T$ at equal loadings (determined using the pure component isotherm fits) across the addressed temperatures. The slope of this plot is equal to Q_{st}/R.

S1.2.6 Numerical Simulation of Breakthrough Curves

The mathematical model used in this work to simulate the transient adsorption behavior of CO_2/CH_4 on MFU-4 is based on the following assumptions:

(i) The gas phase behaves ideally;

(ii) The flow pattern is described by the axially dispersed plug flow model, where the dispersion coefficient is assumed to be constant for all components throughout the bed;

(iii) The superficial velocity is related to the total pressure gradient according through Ergun's equation;

(iv) Radial dispersion is neglected;

(v) The main resistances to mass transfer are combined into a single lumped parameter, where the mass transfer rate is assumed to be linearly dependent of the solid-phase loading, following the Linear Driving Force (LDF) model;[6]

(vi) The adsorbent particles are spherical and homogeneous in size and density. Moreover, they are packed uniformly into the bed. The inter- and intra-particle voidages were set to 0.4 and 0.2, respectively;

(vii) The bed is initially filled with inert He in thermal equilibrium with the feed temperature;

(viii) The physical properties of the gas phase throughout the bed are taken as those of the feed gas;

(ix) The bed operates under isotherm conditions.

The LDF model was adopted due to its simplicity and well-established ability to accurately describe adsorption kinetics in fixed-bed systems. As discussed in the literature, the main features of adsorption kinetics are effectively averaged when describing macroscopic responses such as breakthrough curves, supporting the use of simplified kinetic expressions for this type of analysis.[6] Within this framework, the LDF model represents a lumped mass transfer coefficient and does not explicitly distinguish between different diffusion resistances. Therefore, it provides an effective description of mass transfer processes at the column scale, while maintaining a reduced computational complexity.

According to these assumptions, the governing equations (S4-S7) and correlations (S5.1-S5.5) applied to formulate the one-dimensional fixed bed column model are summarized in Table S1. To numerically solve this model, the Aspen Adsorption v11 package[7] was utilized, which employs the method of lines to solve the time-dependent partial differential equations. The spatial derivatives are discretized over a uniform grid of 200 points using the first-order upwind differencing scheme (UDS-1), combined with Implicit Euler's integration method and a variable time step ranging from 1 to 5 s. The physical properties of the components in the process are locally estimated through integration with the Aspen Properties database.

Table S1. Model equations for fixed bed adsorption simulation.

Fundamental Equations[+]		
Ideal gas law	$(P \times 10^3) y_i = R T_g c_i$	(S4)
Mass balance to adsorbable species	$-\varepsilon_b D_{ax,i} \frac{\partial^2 c_i}{\partial z^2} + \frac{\partial (v_g c_i)}{\partial z} + \varepsilon_t \frac{\partial c_i}{\partial t} + \rho_b \frac{\partial \bar{q}_i}{\partial t} = 0$	(S5)
Momentum balance	$\frac{\partial P}{\partial z} = -\left[\frac{1.5 \times 10^{-4} (1-\varepsilon_b)^2}{(2r_s)^2 \varepsilon_b^3} \mu_g v_g + 1.75 \times 10^{-3} M_g \rho_g \frac{(1-\varepsilon_b)}{2 r_s \varepsilon_b^3} v_g^2\right]$	(S6)
Mass transfer rate	$\frac{\partial \bar{q}_i}{\partial t} = k_{LDF,i}(q_i - \bar{q}_i) \quad , \quad k_{LDF,i} = \frac{k_{LDF\infty,i}}{P} exp\left(\frac{-E_i}{R T_s}\right)$	(S7)
Correlations for estimating transport parameters[*]		
Axial dispersion coefficient	$D_{ax,i} = 0.7 D_{m,i} + 0.5 d_s v_{int}$	(S5.1)
Fairbanks and Wilke correlation	$D_{m,i} = \frac{(1-y_i)}{\sum_{\substack{j=1 \\ j \neq i}}^{N} \frac{y_j}{D_{ij}}}$	(S5.2)
Chapman-Enskog correlation	$D_{ij} = 5.874 \times 10^{-7} \sqrt{T_g^3 \left(\frac{1}{M_i} + \frac{1}{M_j}\right)} \frac{1}{P \sigma_{ij}^2 \Omega_{D_{ij}}}$	(S5.3)
Lennard-Jones parameter	$\sigma_{ij} = \frac{1}{2}(\sigma_i + \sigma_j)$	(S5.4)
Neufeld correlation	$\Omega_{D_{ij}} = \frac{1.06036}{T^{*0.15610}} + \frac{0.19300}{\exp(0.47635 T^*)} + \frac{1.03587}{\exp(1.52996 T^*)} + \frac{1.76474}{\exp(3.89411 T^*)}$ $T^* = \frac{\kappa T_g}{\varepsilon_{ij}} \quad , \quad \frac{\varepsilon_{ij}}{\kappa} = \frac{\sqrt{\varepsilon_i \varepsilon_j}}{\kappa}$	(S5.5)

[+] *The fundamental equations were sourced from the Aspen Adsim™ software library (Aspen Technology, Inc., Version 11.1 – Adsorption Reference Guide);*[7]

[*] *Correlations were referenced as follows: S5.1, from Ruthven;*[4] *S5.2, from Fairbanks and Wilke;*[8] *and the remaining correlations, from Poling et. al;*[9]

All equations and correlations were adjusted to ensure dimensional consistency with the units presented in the nomenclature list;

S1.2.7 Kinetic selectivity and CO_2 working capacity

To ensure a consistent and process-relevant comparison of kinetic CO_2/CH_4 separation performance across all materials, the kinetic selectivity was evaluated using a modified Habgood formulation. In its original form, this formulation combines an adsorption-affinity term, given by the ratio of Henry's constants and strictly valid in the dilute, linear isotherm regime, with the square-root ratio of intracrystalline diffusivities (Eq. S8).[10]

$$S_{CO_2/CH_4} = \frac{K_{CO_2}}{K_{CH_4}} \sqrt{\frac{D_{CO_2}}{D_{CH_4}}} \tag{S8}$$

However, practical adsorption-based separation processes typically operate over finite pressure swings where adsorption isotherms deviate from Henry's law and uptake differences, rather than infinitesimal slopes, govern separation performance. For this reason, a Δq-based affinity term was adopted (Eq. S9), and the resulting kinetic selectivity was calculated accordingly (Eq. S10).[11] This definition captures the effective adsorption capacity accessible within the operating pressure window of interest and provides a more realistic descriptor of adsorption-driven separation under non-dilute conditions. Total pressures of 100 kPa and 500 kPa were selected for the Δq evaluation (loadings taken from the pure-component isotherms), lying outside the strongly nonlinear low-pressure regime and below saturation, thereby providing a representative uptake window for kinetic comparison. Critically, using this fixed pair of total pressures ensures a uniform metric across all materials:

$$\Delta q_i = q_i\left(T_s, P_{high}\right) - q_i(T_s, P_{low}) \tag{S9}$$

$$S_{CO_2/CH_4} = \frac{\Delta q_{CO_2}}{\Delta q_{CH_4}} \sqrt{\frac{D_{CO_2}}{D_{CH_4}}} \tag{S10}$$

The CO_2 working capacities were evaluated using the corresponding CO_2 partial pressures in the mixtures (50:50 and 10:90 CO_2/CH_4), defined as the product of the mixture CO_2 molar fraction and the system total pressure at the same pressure limits (Eq. S11). This ensures consistency between kinetic selectivity and capacity-based performance metrics.

$$WC_{CO_2} = q_{CO_2}\left(T_s, y_{CO_2}P_{high}\right) - q_{CO_2}(T_s, y_{CO_2}P_{low}) \tag{S11}$$

S1.3 Molecular Simulations and Quantum Calculations

The Lennard–Jones parameters and partial atomic charges employed in the molecular simulations to model MFU-4 and the adsorbate molecules are summarized in Tables S2 and S3, respectively.

Table S2. Lennard-Jones parameters for the MFU-4 and CO_2 atoms.

Atom	σ (Å)	ε (K)
Zn_tetrahedral	2.46155	62.39923
Zn_octahedral	2.46155	0.00
C	3.43085	52.83806
N	3.26069	34.72215
H	2.57113	22.14166
Cl	3.51638	114.02384
CO_2_C	2.757	28.129
CO_2_O	3.033	80.507

Table S3. Partial charges of MFU-4 and CO_2 atoms calculated using DDEC6 method.

Atom	q (e)
Zn_tetrahedral	0.5885
Zn_octahedral	0.4375
C (bonded to N)	0.1336
C (bonded to H)	-0.2084
N_central	0.0104
N_peripheral	-0.1945
H	0.1459
Cl	-0.4372
CO_2_C	0.6512
CO_2_O	-0.3256

S2. Results

S2.1 Single-Component Adsorption

Breakthrough experiments were performed on CO_2 in MFU-4 to determine its adsorption equilibrium isotherms. The experimental conditions and calculated loadings are summarized in Table S4, while the breakthrough curves are displayed in Figure S8. In each panel of the figure, the effect of temperature is shown for a constant partial pressure. To support the molecular-level interpretation of the experimental adsorption data, GCMC simulations were employed to describe CO_2 adsorption in MFU-4 and to enable direct comparison between experimental and computational isotherms. The corresponding CO_2 adsorption isotherms obtained from these

simulations are discussed in the main text, where they are directly compared with the experimental breakthrough-derived isotherms. The force field employed in the GCMC simulations was benchmarked by comparing radial distribution functions (RDFs) obtained from NVT Monte Carlo and ab initio molecular dynamics (AIMD) simulations, as shown in Figure S9, demonstrating good agreement between the two approaches. Figure S10 presents representative snapshots from GCMC simulations of CO_2 adsorption in MFU-4 at 298 K and pressures of 10 and 500 kPa.

Table S4. Experimental conditions for measuring single component breakthrough curves for CO_2 on MFU-4.

RUN	Temp (K)	Total pressure (kPa)	CO_2 partial pressure (kPa)	He flowrate ($mL \cdot min^{-1}$)	CO_2 flowrate ($mL \cdot min^{-1}$)	CO_2 loading ($mol \cdot kg^{-1}$)
1_1	298	100	5.09×10^{1}	1.67×10^{0}	1.73×10^{0}	1.95×10^{0}
1_2	298	200	1.02×10^{2}	3.23×10^{0}	3.38×10^{0}	3.61×10^{0}
1_3	298	300	1.51×10^{2}	4.80×10^{0}	4.85×10^{0}	4.60×10^{0}
1_4	298	400	2.13×10^{2}	6.49×10^{0}	7.41×10^{0}	5.44×10^{0}
1_5	298	300	3.00×10^{2}	-	1.04×10^{1}	6.46×10^{0}
1_6	298	400	4.00×10^{2}	-	1.35×10^{1}	6.86×10^{0}
1_7	298	500	5.00×10^{2}	-	1.67×10^{1}	7.36×10^{0}
1_8	313	100	5.35×10^{1}	1.50×10^{0}	1.73×10^{0}	1.37×10^{0}
1_9	313	200	9.97×10^{1}	3.14×10^{0}	3.12×10^{0}	2.39×10^{0}
1_10	313	300	1.48×10^{2}	4.80×10^{0}	4.70×10^{0}	3.36×10^{0}
1_11	313	400	2.14×10^{2}	6.20×10^{0}	7.14×10^{0}	4.23×10^{0}
1_12	313	300	3.00×10^{2}	-	9.73×10^{0}	5.12×10^{0}
1_13	313	400	4.00×10^{2}	-	1.29×10^{1}	5.86×10^{0}
1_14	313	500	5.00×10^{2}	-	1.60×10^{1}	6.33×10^{0}
1_15	343	100	5.14×10^{1}	1.40×10^{0}	1.49×10^{0}	6.11×10^{-1}
1_16	343	200	9.81×10^{1}	2.86×10^{0}	2.76×10^{0}	1.01×10^{0}
1_17	343	300	1.51×10^{2}	4.27×10^{0}	4.33×10^{0}	1.62×10^{0}
1_18	343	400	2.19×10^{2}	5.66×10^{0}	6.85×10^{0}	2.39×10^{0}
1_19	343	300	3.00×10^{2}	-	8.68×10^{0}	3.09×10^{0}
1_20	343	400	4.00×10^{2}	-	1.18×10^{1}	3.80×10^{0}
1_21	343	500	5.00×10^{2}	-	1.47×10^{1}	4.31×10^{0}

The mass of MFU-4 packed in the column is around 266 mg;
The flowrates are expressed at the standard temperature and pressure (STP) conditions.

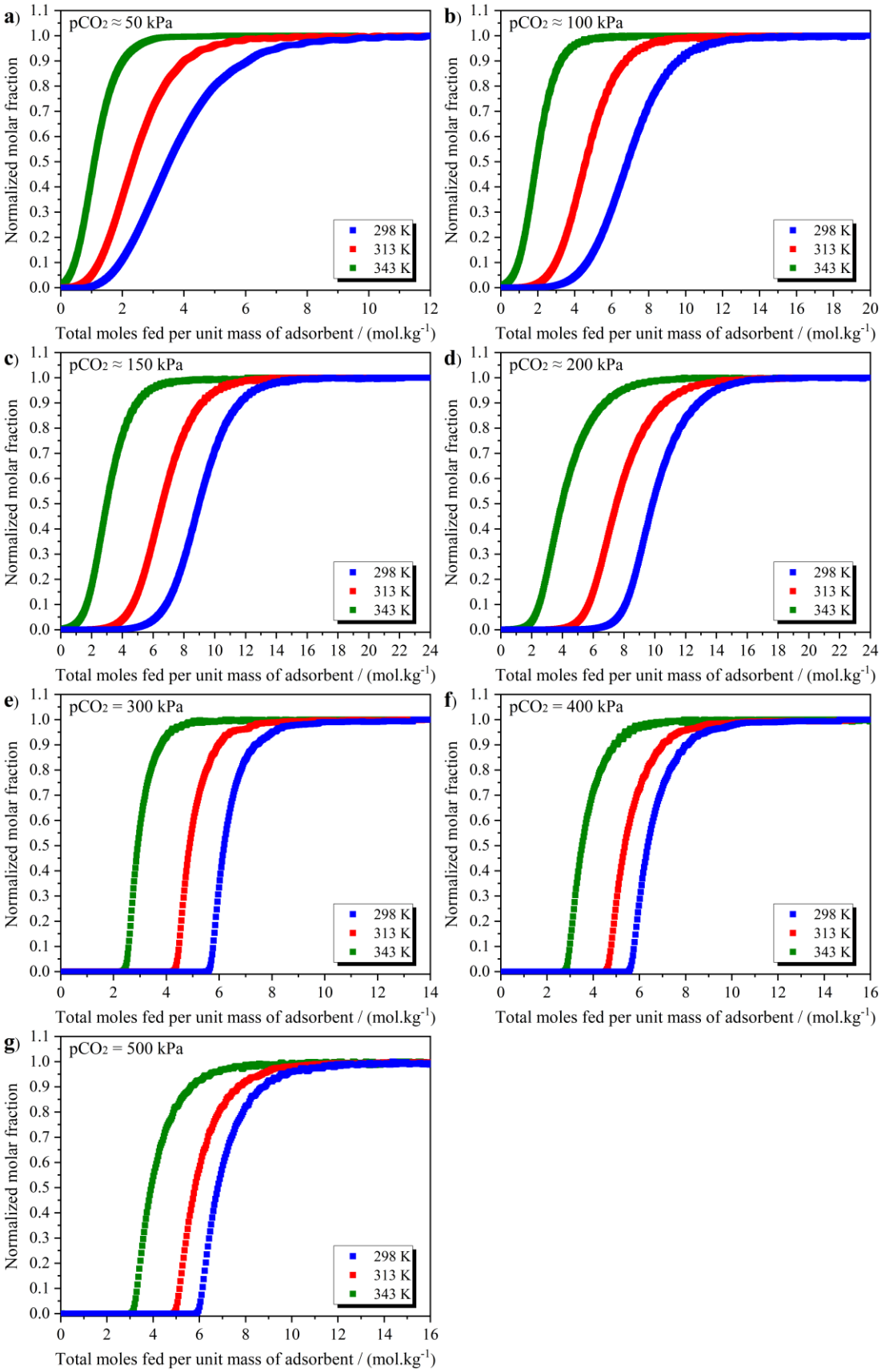

Figure S8. Single-component breakthrough curves on CO_2 in MFU-4 in the temperature range of 298-343 K: **(a)** 50 kPa, **(b)** 100 kPa, **(c)** 150 kPa, **(d)** 200 kPa, **(e)** 300 kPa, **(f)** 400 kPa, and **(g)** 500 kPa. Data are plotted as normalized molar fraction of CO_2 (left *y*-axis) versus total moles fed per unit mass of adsorbent.

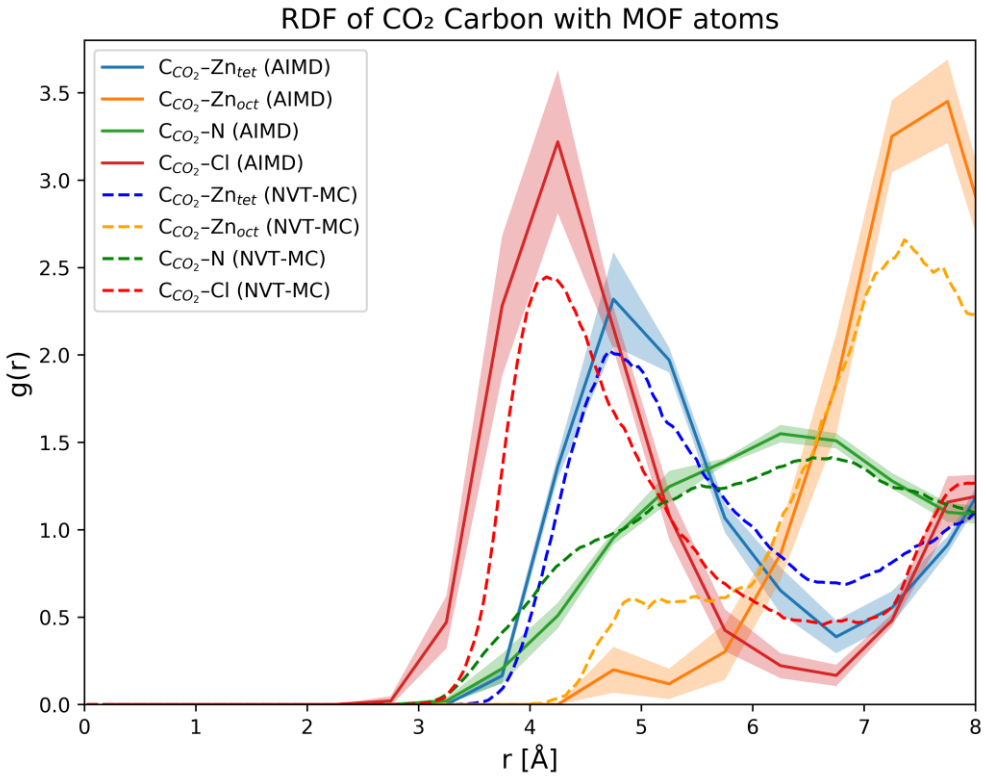

Figure S9. Radial distribution functions (RDFs) between the carbon atom of CO_2 and selected framework atoms of MFU-4 (tetrahedral Zn, octahedral Zn, N, and Cl) obtained from AIMD (solid lines) and NVT Monte Carlo (dotted lines) simulations. The AIMD results are averaged over four independent trajectories, with the shaded regions indicating the corresponding standard deviations. The close agreement between the DFT-based AIMD and classical Monte Carlo RDFs supports the suitability of the employed force field for describing CO_2 adsorption in MFU-4.

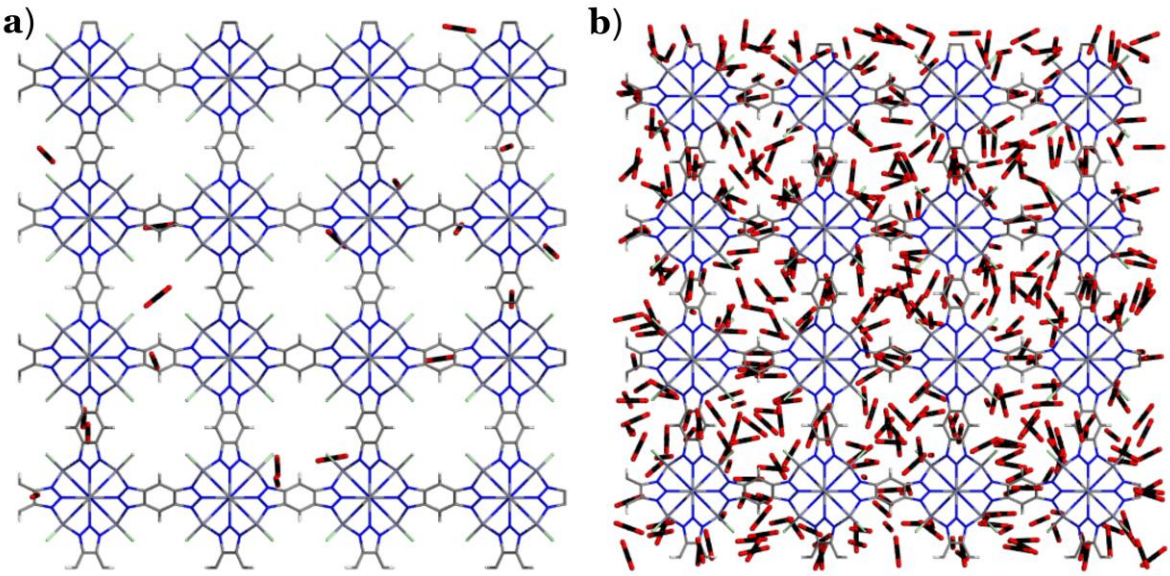

Figure S10. Representative snapshots from GCMC simulations of CO_2 adsorption in MFU-4 at 298 K: **(a)** 10 kPa and **(b)** 500 kPa.

Having validated the simulation methodology against CO_2 adsorption, the same computational approach was subsequently applied to investigate CH_4 adsorption in MFU-4. In contrast to CO_2, the simulated CH_4 isotherms (Figure S11a) exhibit an approximately linear dependence on pressure, indicating a markedly lower affinity for the framework. The predicted equilibrium uptakes confirm that CH_4 adsorption is thermodynamically allowed but intrinsically limited. Representative adsorption snapshots (Figure S11b) reveal weaker host–guest interactions, with CH_4 heterogeneously distributed within the cages. Table S5 compiles the simulated equilibrium adsorption capacities of both CO_2 and CH_4 used to construct the corresponding isotherms.

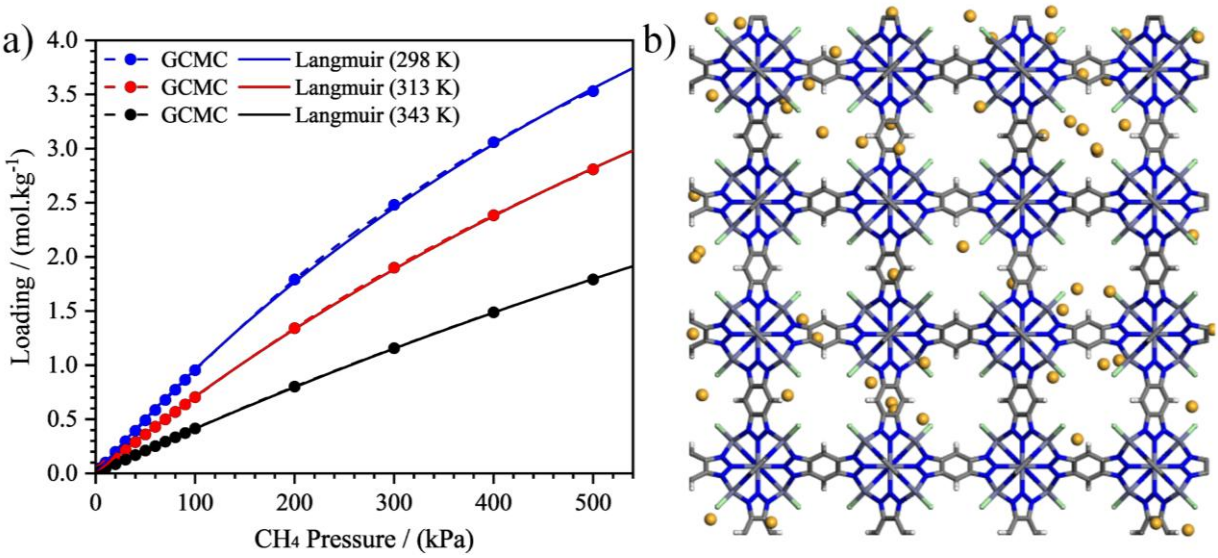

Figure S11. (a) Equilibrium single-component CH_4 adsorption isotherms on MFU-4 in the temperature range of 298–343 K. Symbols and dashed correspond to GCMC simulations, and continuous lines represent the Langmuir thermodynamic model fit. **(b)** Representative snapshot from a GCMC simulation of CH_4 adsorption in MFU-4 at 298 K and 100 kPa.

Table S5. GCMC-predicted equilibrium single-component adsorption equilibrium loadings of CO_2 and CH_4 on MFU-4.

partial pressure (kPa)	CO_2 (298 K) ($mol \cdot kg^{-1}$)	CH_4 (298 K) ($mol \cdot kg^{-1}$)	CO_2 (313 K) ($mol \cdot kg^{-1}$)	CH_4 (313 K) ($mol \cdot kg^{-1}$)	CO_2 (343 K) ($mol \cdot kg^{-1}$)	CH_4 (343 K) ($mol \cdot kg^{-1}$)
1.00×10^{-3}	5.00×10^{-5}	1.00×10^{-5}	3.00×10^{-5}	1.00×10^{-5}	1.00×10^{-5}	0.00×10^{0}
5.00×10^{-3}	2.40×10^{-4}	5.00×10^{-5}	1.50×10^{-4}	4.00×10^{-5}	7.00×10^{-5}	2.00×10^{-5}
1.00×10^{-2}	4.80×10^{-4}	1.00×10^{-4}	3.10×10^{-4}	7.00×10^{-5}	1.40×10^{-4}	4.00×10^{-5}
5.00×10^{-2}	2.35×10^{-3}	5.00×10^{-4}	1.50×10^{-3}	3.70×10^{-4}	7.00×10^{-4}	2.20×10^{-4}
1.00×10^{-1}	4.66×10^{-3}	1.00×10^{-3}	2.98×10^{-3}	7.30×10^{-4}	1.40×10^{-3}	4.30×10^{-4}
5.00×10^{-1}	2.26×10^{-2}	4.99×10^{-3}	1.46×10^{-2}	3.66×10^{-3}	6.86×10^{-3}	2.13×10^{-3}
1.00×10^{0}	4.52×10^{-2}	9.96×10^{-3}	2.90×10^{-2}	7.32×10^{-3}	1.35×10^{-2}	4.27×10^{-3}
5.00×10^{0}	2.24×10^{-1}	4.98×10^{-2}	1.43×10^{-1}	3.65×10^{-2}	6.68×10^{-2}	2.13×10^{-2}
1.00×10^{1}	4.48×10^{-1}	9.92×10^{-2}	2.86×10^{-1}	7.29×10^{-2}	1.33×10^{-1}	4.26×10^{-2}
2.00×10^{1}	8.92×10^{-1}	1.98×10^{-1}	5.69×10^{-1}	1.45×10^{-1}	2.66×10^{-1}	8.48×10^{-2}
3.00×10^{1}	1.33×10^{0}	2.96×10^{-1}	8.48×10^{-1}	2.17×10^{-1}	3.97×10^{-1}	1.27×10^{-1}
4.00×10^{1}	1.76×10^{0}	3.93×10^{-1}	1.13×10^{0}	2.89×10^{-1}	5.29×10^{-1}	1.69×10^{-1}
5.00×10^{1}	2.19×10^{0}	4.90×10^{-1}	1.40×10^{0}	3.59×10^{-1}	6.54×10^{-1}	2.10×10^{-1}
6.00×10^{1}	2.59×10^{0}	5.85×10^{-1}	1.68×10^{0}	4.30×10^{-1}	7.85×10^{-1}	2.52×10^{-1}
7.00×10^{1}	2.99×10^{0}	6.78×10^{-1}	1.94×10^{0}	4.99×10^{-1}	9.09×10^{-1}	2.93×10^{-1}
8.00×10^{1}	3.38×10^{0}	7.72×10^{-1}	2.19×10^{0}	5.68×10^{-1}	1.03×10^{0}	3.33×10^{-1}
9.00×10^{1}	3.72×10^{0}	8.63×10^{-1}	2.46×10^{0}	6.36×10^{-1}	1.16×10^{0}	3.73×10^{-1}
1.00×10^{2}	4.01×10^{0}	9.53×10^{-1}	2.69×10^{0}	7.04×10^{-1}	1.28×10^{0}	4.14×10^{-1}
2.00×10^{2}	5.94×10^{0}	1.79×10^{0}	4.55×10^{0}	1.34×10^{0}	2.40×10^{0}	8.02×10^{-1}
3.00×10^{2}	6.71×10^{0}	2.48×10^{0}	5.60×10^{0}	1.90×10^{0}	3.33×10^{0}	1.16×10^{0}
4.00×10^{2}	7.14×10^{0}	3.06×10^{0}	6.20×10^{0}	2.38×10^{0}	4.06×10^{0}	1.49×10^{0}
5.00×10^{2}	7.41×10^{0}	3.53×10^{0}	6.61×10^{0}	2.81×10^{0}	4.62×10^{0}	1.79×10^{0}

The thermodynamic Langmuir isotherm model was employed to fit the adsorption equilibrium isotherms. To model parameters were determined by minimizing the sum of squared errors (ERRSQ) between the experimental CO_2 data (Table S4) or GCMC-simulated CH_4 data (Table S5) and the corresponding model predictions, which served as the convergence criterion.[12] Analysis of the configurational GCMC data reveals that CO_2 adsorbs at two distinct sites within MFU-4, whereas CH_4 occupies a single type of site. Accordingly, a dual-site model was applied for CO_2, while a single-site model was used for CH_4. The optimized fitting parameters are reported in Table S6.

Table S6. Fitted Langmuir model parameters for CO_2 and CH_4 on MFU-4.

Parameters		CO_2	CH_4
q_{sat_1}	($mol \cdot kg^{-1}$)	5.37×10^{0}	1.10×10^{1}
q_{sat_2}	($mol \cdot kg^{-1}$)	6.38×10^{0}	-
$b_{1,\infty}$	(kPa^{-1})	1.76×10^{-5}	1.03×10^{-4}
$b_{2,\infty}$	(kPa^{-1})	2.03×10^{-5}	-
$-\Delta H_1$	($J \cdot mol^{-1}$)	2.48×10^{4}	1.69×10^{4}
$-\Delta H_2$	($J \cdot mol^{-1}$)	2.46×10^{4}	-

The Q_{st} profiles derived from the Clausius–Clapeyron relation (Eq. S3) are shown in Figure S12. Both CO_2 and CH_4 exhibit essentially constant values over the investigated loading range. For CO_2, Q_{st} remains at ~24.9 $kJ \cdot mol^{-1}$, reflecting the similarity of the adsorption enthalpies and affinities of the two sites, which results in a coverage-independent behavior. For CH_4, the corresponding value is ~16.9 $kJ \cdot mol^{-1}$, indicating uniformly host-guest interactions with the framework (typical of a single-site model). In agreement with these results, the simulated zero-coverage adsorption enthalpy of CH_4 is ~16 $kJ \cdot mol^{-1}$. The analysis of Q_{st} was restricted to the maximum loading experimentally observed for CO_2 or simulated for CH_4 at 343 K, avoiding model-driven extrapolation and ensuring that the Clausius–Clapeyron equation is confined to the range where the fitted parameters are validated.[5]

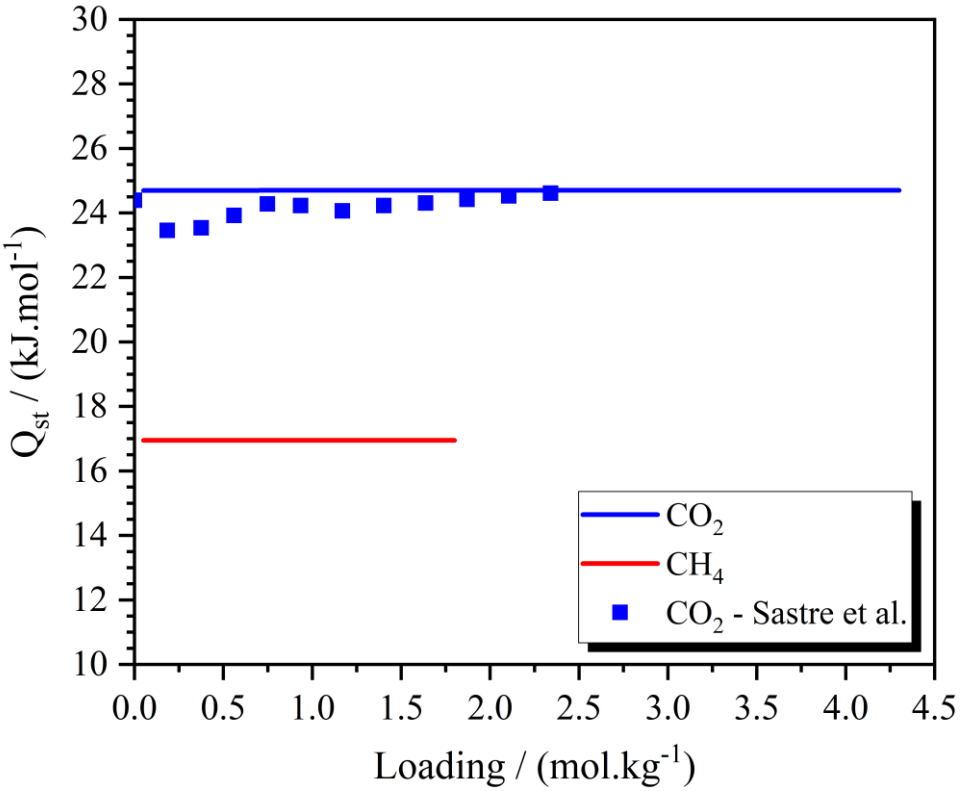

Figure S12. Q_{st} profiles for CO_2 and CH_4 on MFU-4 as a function of loading. Continuous lines correspond to data from this work, and symbols represent data from Sastre et al.[13]

S2.2 Multi-Component Adsorption

The multicomponent breakthrough experiments for CO_2/CH_4 binary mixtures were carried out at 100 and 500 kPa using two feed compositions (90:10 and 50:50) to evaluate the adsorption separation performance of MFU-4. The experimental conditions and calculated loadings are summarized in Table S7, while the breakthrough curves at 313 and 343 K are shown in Figures S13 and S14, respectively. With increasing temperature, the qualitative features of the breakthrough profiles remain unchanged: CH_4 continues to elute at the space time of the gas in the bed, whereas CO_2 is selectively adsorbed.

To further evaluate the stability of MFU-4 under cyclic operation, a series of ten consecutive adsorption–desorption cycles were performed at 298 K for a CO_2/CH_4 (50:50 vol.%) mixture at total pressures of 100 and 500 kPa under the same operating conditions used in the breakthrough experiments (Figure 3, main text). For both cases, desorption was carried out using He at identical temperature, pressure, and total flowrate.

The results are presented in Figure S15, where panels (a) and (c) show the consecutive cycles as a function of continuous time, while panels (b) and (d) display the corresponding curves superimposed as a function of cycle time. At 100 kPa, adsorption and desorption steps were both performed with a duration of 10 min, whereas at 500 kPa, adsorption was maintained at 10 min

and desorption extended to 20 min to ensure complete regeneration of the material. In all cases, highly reproducible breakthrough curves are observed over successive cycles, confirming the stability of the adsorption performance. The CO_2 uptake remains essentially constant throughout the cycles, indicating the absence of capacity loss. In addition, the desorption profiles clearly show that CH_4 is not retained in the material, as its mole fraction in the outlet stream rapidly decreases to zero at the beginning of the desorption step. These results demonstrate that MFU-4 can be fully regenerated under mild conditions without the need for vacuum or temperature swing, even at elevated pressure (500 kPa). The complete desorption observed under these conditions indicates that regeneration is not limited by pressure and would be further facilitated under lower-pressure operation. In addition, no accumulation of CH_4 occurs within the framework.

Table S7. Experimental conditions for measuring multicomponent breakthrough curves for binary CO_2/CH_4 mixtures on MFU-4.

RUN	Temp (K)	Total pressure (kPa)	CO_2 flowrate ($mL \cdot min^{-1}$)	CH_4 flowrate ($mL \cdot min^{-1}$)	CO_2 loading ($mol \cdot kg^{-1}$)
≈50% CO_2 – 50% CH_4					
2_1	298	100	3.30×10^{0}	3.38×10^{0}	1.91
2_2	298	500	9.50×10^{0}	8.62×10^{0}	6.06
2_3	313	100	3.03×10^{0}	3.13×10^{0}	1.24
2_4	313	500	9.07×10^{0}	8.05×10^{0}	4.84
2_5	343	100	2.84×10^{0}	2.87×10^{0}	0.553
2_6	343	500	8.00×10^{0}	7.20×10^{0}	2.93
≈10% CO_2 – 50% CH_4					
3_1	298	100	8.90×10^{-1}	6.09×10^{0}	0.538
3_2	298	500	2.27×10^{0}	1.47×10^{1}	2.24
3_3	313	100	8.10×10^{-1}	5.78×10^{0}	0.317
3_4	313	500	2.16×10^{0}	1.44×10^{1}	1.40
3_5	343	100	7.20×10^{-1}	5.19×10^{0}	0.102
3_6	343	500	2.13×10^{0}	1.31×10^{1}	0.773

The mass of MFU-4 packed in the column is around 266 mg;

The flowrates are expressed at the standard temperature and pressure (STP) conditions.

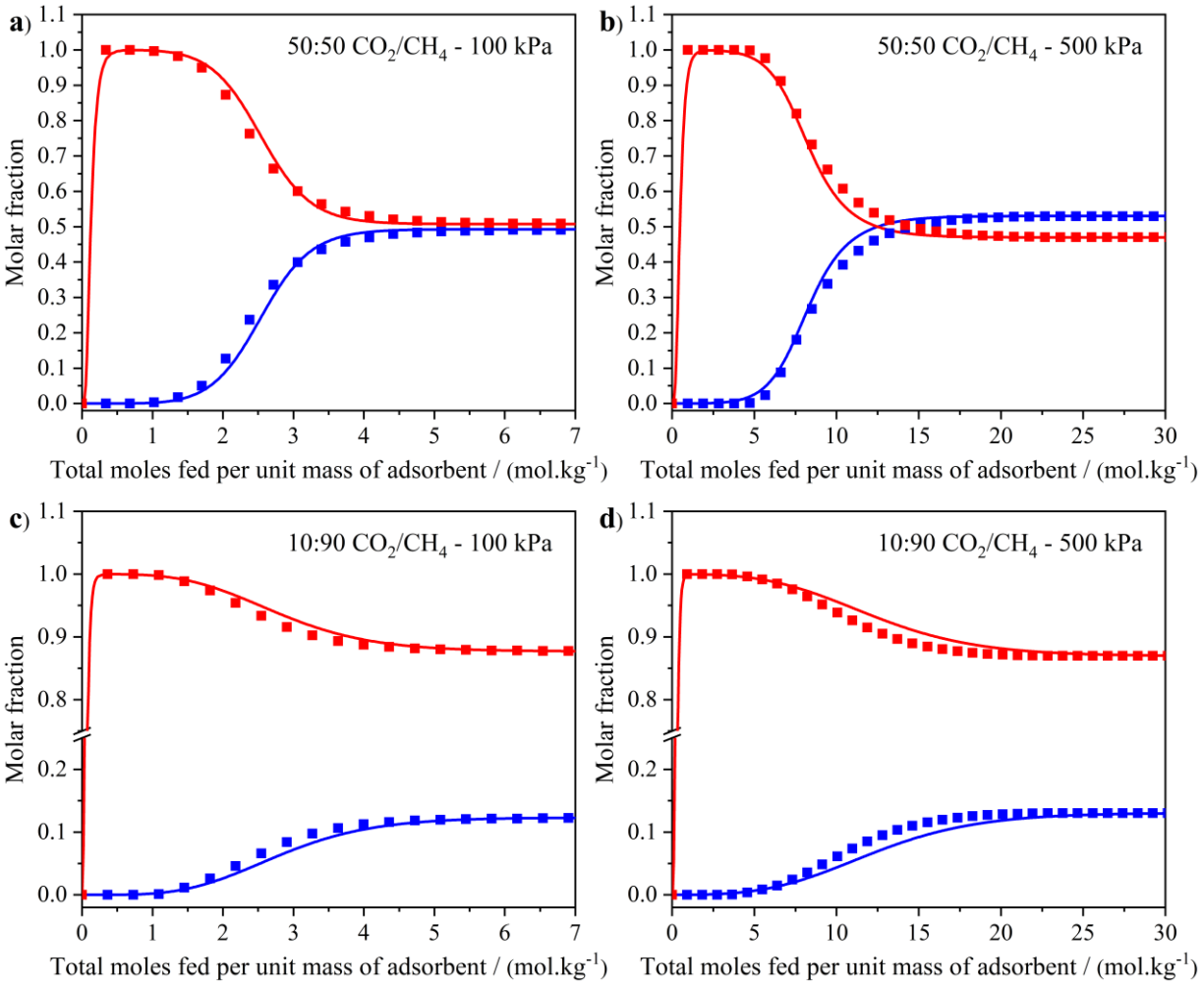

Figure S13. Binary breakthrough curves for CO_2/CH_4 mixtures on MFU-4 at 313 K. Conditions for each panel are: (a) CO_2/CH_4 50:50 at 100 kPa, **(b)** CO_2/CH_4 50:50 at 500 kPa, **(c)** CO_2/CH_4 10:90 at 100 kPa, and **(d)** CO_2/CH_4 10:90 at 500 kPa. Data are plotted as component molar fraction (left *y*-axis) versus total moles fed per unit mass of adsorbent. Symbols represent experimental data, and continuous lines represent numerical simulations.

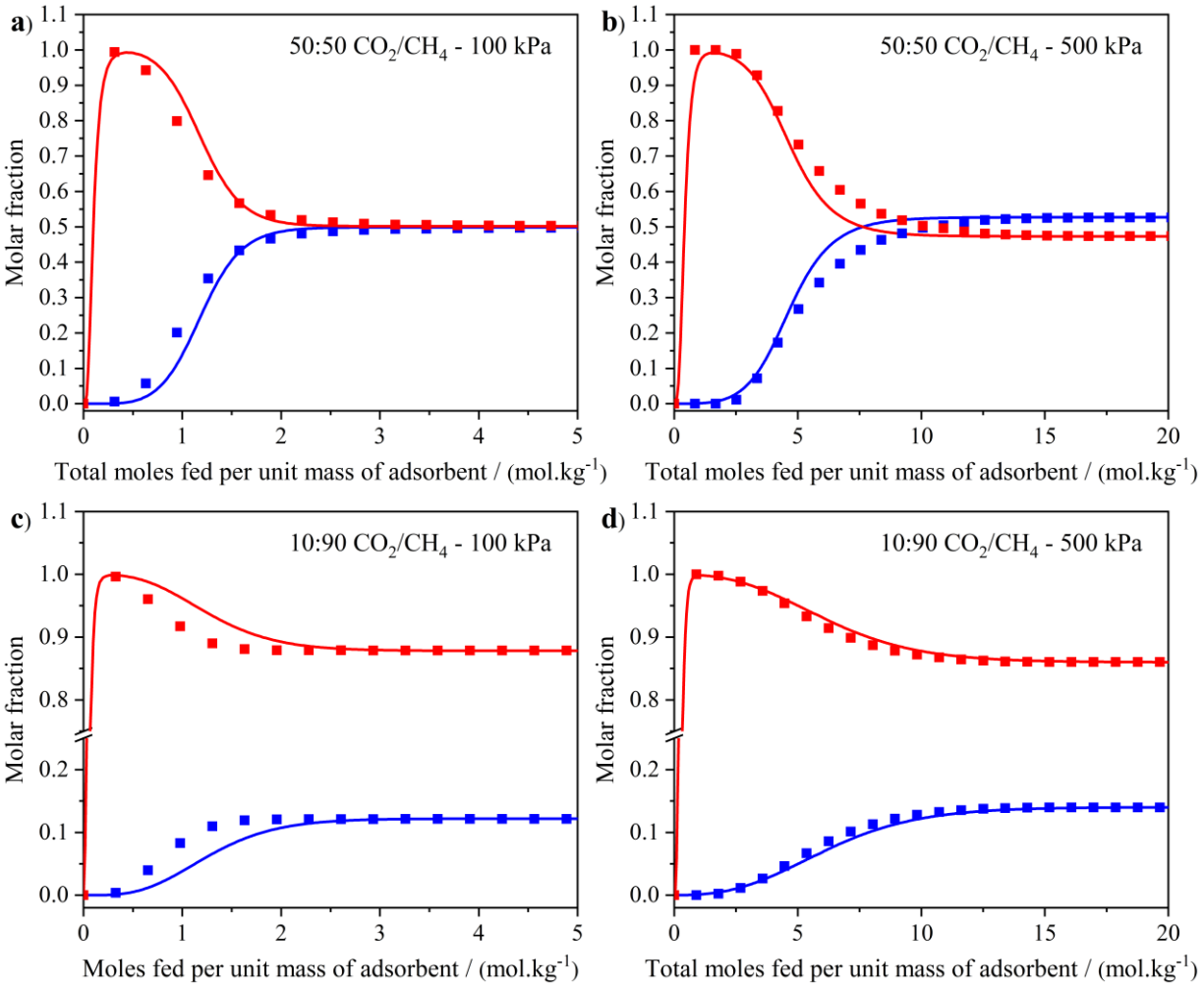

Figure S14. Binary breakthrough curves for CO_2/CH_4 mixtures on MFU-4 at 343 K. Conditions for each panel are: (a) CO_2/CH_4 50:50 at 100 kPa, **(b)** CO_2/CH_4 50:50 at 500 kPa, **(c)** CO_2/CH_4 10:90 at 100 kPa, and **(d)** CO_2/CH_4 10:90 at 500 kPa. Data are plotted as component molar fraction (left *y*-axis) versus total moles fed per unit mass of adsorbent. Symbols represent experimental data, and continuous lines represent numerical simulations.

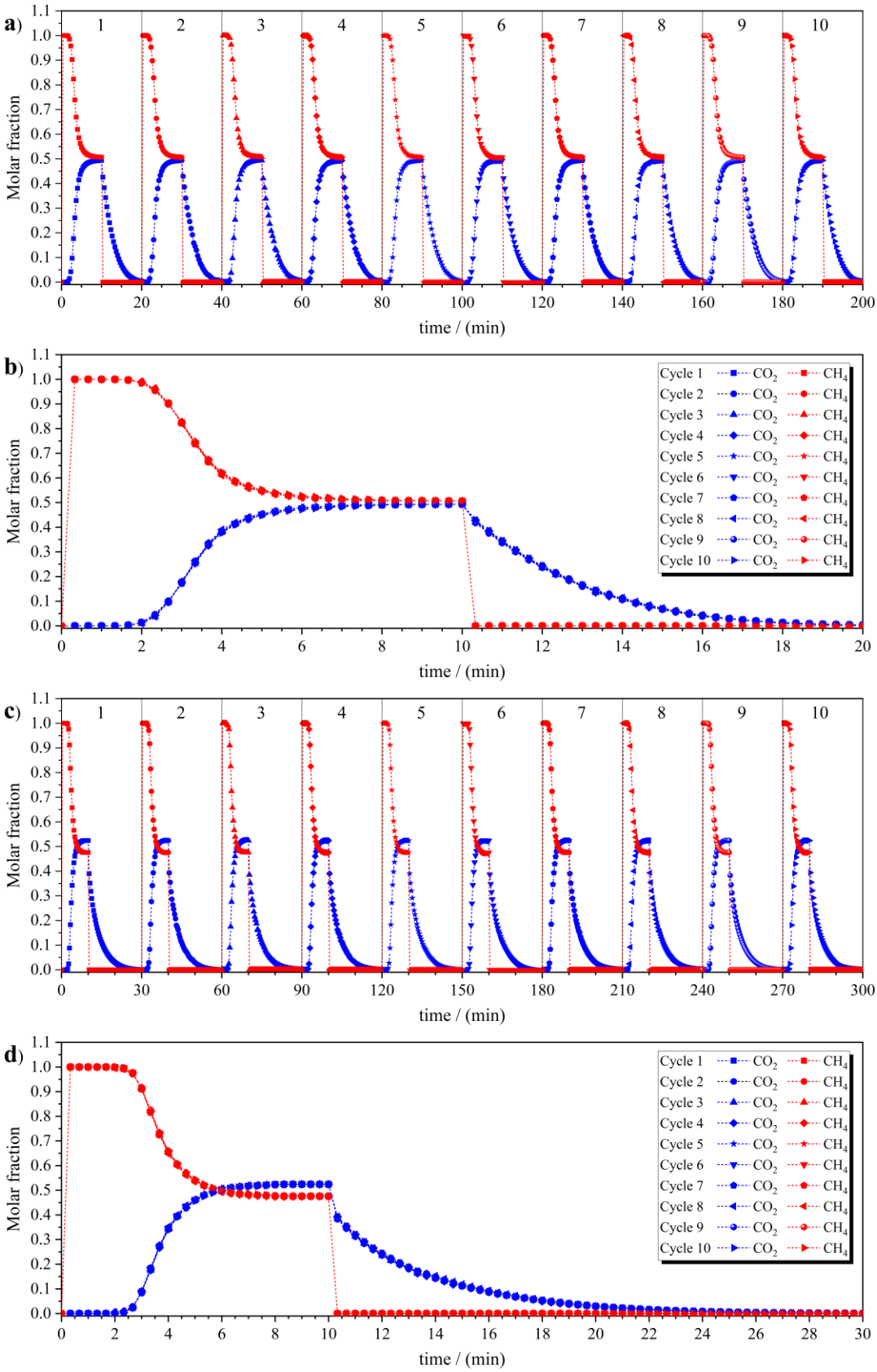

Figure S15. Consecutive adsorption–desorption breakthrough cycles for a CO_2/CH_4 (50:50 vol.%) mixture on MFU-4 at 298 K and total pressures of (a,b) 100 kPa and **(c,d)** 500 kPa. Panels **(a)** and **(c)** show the cycles as a function of continuous time, while panels **(b)** and **(d)** display the corresponding curves superimposed as a function of cycle time.

To quantitatively describe the dynamic separation behavior and extract diffusion parameters, the experimental breakthrough curves were modeled using Aspen Adsorption. The fitted parameters of the pressure-dependent Arrhenius-type kinetic expression (Eq. S7) that best reproduce the experimental profiles are reported in Table S8.

Table S8. Mass transfer coefficients for CO_2 and CH_4 on MFU-4.

Arrhenius Model		CO_2		CH_4	
k_∞	(kPa·s^{-1})	6.37×10^3		4.25×10^0	
E_i	(J·mol^{-1})	1.50×10^3		1.50×10^3	
		100 kPa	500 kPa	100 kPa	500 kPa
k_{LDF} (298 K)	(s^{-1})	1.50×10^{-1}	3.00×10^{-2}	≤ 1.00×10^{-4}	≤ 2.00×10^{-5}
k_{LDF} (313 K)	(s^{-1})	2.00×10^{-1}	4.01×10^{-2}	≤ 1.34×10^{-4}	≤ 2.67×10^{-5}
k_{LDF} (343 K)	(s^{-1})	3.32×10^{-1}	6.63×10^{-2}	≤ 2.21×10^{-4}	≤ 4.42×10^{-5}

Table S9 reports the CO_2 working capacities for all evaluated materials, CMS-3K, Sr-ETS-4, Ba-ETS-4, and MFU-4, together with the diffusion time constants, D_i/r_c^2, of CO_2 and CH_4 used to calculate $S_{kinetic}$. The CO_2/CH_4 loadings for each material, at total pressures of 100 kPa and 500 kPa selected for the Δq evaluation, as well as the mixture working capacities, were obtained from their respective isotherm fits. All D_i/r_c^2 listed in Table S9 were determined at 100 kPa. Although, for MFU-4, the fitted k_{LDF} values exhibited pressure dependence as suggested by Aspen Adsorption, this does not affect the calculation of $S_{kinetic}$ (Eq. S8), since only the ratio of the diffusion constants is required, and this ratio remains invariant. For consistency with the literature data compiled in Table S9, the k_{LDF} obtained in this work (Table S8) were converted using the classical relation $k_{LDF} = 15D_i/r_c^2$. This factor of 15 originates from the analytical solution for transient diffusion in spherical particles, an assumption consistent with the particle geometry adopted the simulations. Even if the exact proportionality factor differed slightly, the resulting kinetic selectivity would remain unchanged, as it depends solely on the ratio between the CO_2 and CH_4 diffusion constants.

Within the ETS-4 family, the highest ideal kinetic selectivities reported in the literature were originally obtained for N_2/CH_4 systems. Classical studies demonstrated that Sr- and Ba-exchanged ETS-4 in their dehydrated forms exhibit much stronger diffusional restrictions for CH_4 than the parent Na-ETS-4 framework.[14,15] Although these measurements were performed for N_2/CH_4 mixtures, the underlying mechanism, thermally induced channel contraction that disproportionately hinders CH_4 transport, is equally relevant for CO_2/CH_4 discrimination. For

this reason, Sr- and Ba-exchanged ETS-4 are the most appropriate framework representatives for benchmarking kinetic CO_2/CH_4 separation. Accordingly, the equilibrium adsorption data of CO_2 and CH_4, as well as the CO_2 diffusivities, were taken from a recent ion-exchanged ETS-4 study that identifies the dehydration regime yielding the highest CO_2/CH_4 equilibrium selectivity for each exchanged form.[16] The corresponding CH_4 diffusivities were sourced from the classical kinetic studies under matching dehydration conditions, ensuring structural and thermodynamic consistency across all datasets. This procedure provides a coherent basis for comparing the kinetic CO_2/CH_4 performance of ETS-4 with that of MFU-4.

Table S9. Comparison of CO_2 working capacities and ideal kinetic selectivities at near ambient temperature for ETS-4 variants, CMS-3K, and MFU-4.

	CO_2 working capacity		Diffusional time constants		$S_{kinetic}$
	50:50 CO_2/CH_4 ($mol \cdot kg^{-1}$)	10:90 CO_2/CH_4 ($mol \cdot kg^{-1}$)	D_{CO_2}/r_c^2 (s^{-1})	D_{CH_4}/r_c^2 (s^{-1})	
CMS-3K	0.942	0.785	1.05×10^{-3}	$\leq 2.33\times10^{-6}$	≥15.6
Sr-ETS-4	0.576	0.360	2.12×10^{-3}	$\leq 1.30\times10^{-5}$	≥26.6
Ba-ETS-4	0.562	0.425	2.03×10^{-3}	$\leq 6.06\times10^{-6}$	≥35.5
MFU-4	3.93	1.52	1.00×10^{-2}	$\leq 6.67\times10^{-6}$	≥66.8

The diffusion constants D_i/r_c^2, as well as the CO_2 working capacities collected from the literature, were in some cases reported at temperatures slightly different from 298 K. However, the deviations from room temperature are minimal, and both the loadings and the diffusion constants remain within the same order of magnitude. As such, these small temperature differences do not significantly affect the kinetic selectivity.

CO_2 working capacities and diffusional constants for ETS-4 (293 K);[16]

CH_4 diffusional constants for ETS-4 (283 K);[14,15]

CO_2 working capacities and CO_2/CH_4 diffusional constants for CMS-3K (298K, 308 K);[11]

CO_2 working capacity and CO_2/CH_4 diffusional constants for MFU-4 (298 K), this work.

S2.3. Benchmarking of MFU-4 Against Reported Adsorbents

A literature survey was conducted to benchmark the performance of MFU-4 against representative examples from different classes of porous materials, as summarized in Table S10. The materials surveyed include activated carbons (AC), carbon molecular sieves (CMS), other MOFs, pillared clays (PILCs), periodic mesoporous organosilicas (PMOs), silicas, and zeolites. All entries in Table S10 were evaluated for CO_2/CH_4 separation, and the selected materials are intended to be representative of each material class. The comparison was performed at

temperatures in the range of 298 ± 5 K. The key parameters analyzed include the CO_2 uptake (q_{CO_2}) at 100 and 500 kPa, the isosteric heat of adsorption of CO_2 (Q_{st,CO_2}), and the CO_2/CH_4 selectivity (S_{CO_2/CH_4}). Selectivity values were considered from: (i) Ideal Adsorbed Solution Theory (IAST), reported either as average selectivities or as composition-dependent values for gas mixtures with CO_2:CH_4 ratios of (50 ± 10):(50 ± 10) vol.%; (ii) binary breakthrough experiments conducted under similar CO_2:CH_4 compositions; and (iii) the Habgood formulation (Equation S10). Alongside these quantitative parameters, the materials are also classified according to their dominant separation mechanism. Whenever available, data are reported as presented in the original references. Otherwise, values were derived from fitting parameters reported in the literature or estimated through digitization of published figures using the PlotDigitizer online tool.

Table S10. Benchmarking of the CO_2/CH_4 separation performance of MFU-4 against literature-reported adsorbent materials.

Type	Material	Form	T. (K)	q_{CO_2} (mol/kg)		Q_{st,CO_2} (kJ/mol)	S_{CO_2/CH_4} (-)	Separation Mechanism CO_2/CH_4	Reference
				100 kPa	500 kPa				
AC	Maxsorb [1]	n.s	298	1.92	6.42	19.7-24.0	-	thermodynamic	[17]
	CS-CO_2 [2]	n.s.	303	2.32	4.96	20.3-23.5	3.70 (100 kPa) 3.95 (500 kPa)	thermodynamic	[18]
	CS-H_2O [2]			2.30	4.83	22.4-25.7	4.00 (100 kPa) 4.07 (500 kPa)		
	Calgon BPL [3]	n.s.	303	1.69	4.52	-	3.58 (100 kPa) 3.33 (500 kPa)	thermodynamic	[19]
	Pine-sawdust [4]	pellet	303	2.53	4.48	24.2	5.23 (120 kPa) 3.93 (500 kPa)	thermodynamic	[20]
CMS	3K-161 [5]	pellet	298	1.84	2.79	-	15.6	kinetic	[11]
	KP-407 [6]	pellet	298	1.86	3.06	-	12.0	kinetic	[21]
	Shirasagi MSC CT-350 [7]	pellet	293	2.03	3.23	-	46.7	kinetic	[22]
MOF	Mg-MOF-74 [8]	powder	298	8.32	12.9	45.3-72.7	-	thermodynamic	[23]
	UTSA-16 [9]	powder	296	4.36	5.09	≈33.5	35.9 (100 kPa)	thermodynamic	[24]
	CAU-10-H [10]	powder	303	2.30	4.08	-	4.9 (100 kPa)	thermodynamic	[25]
	CAU-10-OH [10]			1.07	2.18		3.5 (100 kPa)		
	CAU-10-NH_2 [10]			1.82	3.11		4.4 (100 kPa)		
	CAU-10-NO_2 [10]			1.95	3.24		8.0 (100 kPa)		
	CAU-10-OCH_3 [10]			0.81	2.07		1.7 (100 kPa)		
	CAU-10-CH_3 [10]			1.21	2.87		3.0 (100 kPa)		
	Cu-BTC [11]	n.s.	303	4.55	11.7	30	-	thermodynamic	[26]
	UiO-66(Zr) [11]			1.34	3.86	27			
	UiO-66(Zr)-NH_2 [11]			2.69	5.35	31-35			
	MIL-125(Ti) [11]			1.79	6.63	26			

Table S10 (*cont.*). Benchmarking of the CO_2/CH_4 separation performance of MFU-4 against literature-reported adsorbent materials.

Type	Material	Form	T. (K)	q_{CO_2} (mol/kg)		Q_{st,CO_2} (kJ/mol)	S_{CO_2/CH_4} (-)	Separation Mechanism CO_2/CH_4	Reference
				100 kPa	500 kPa				
MOF	MIL-125(Ti)-NH_2 [11]	n.s.	303	2.64	6.84	30	-	thermodynamic	[26]
	MIL-100(Fe) [11]			3.15	7.22	22-37			
	MIL-100(Cr) [11]			3.50	8.08	21-35			
	NH_2-MIL-53(Al) [12]	powder	303	1.97	2.39	32	207 (100 kPa) 19 (500 kPa)	Near sieving (≤100 kPa) thermodynamic (≥500kPa)	[27]
	ZJU-8a [13]	powder	298	4.18	10.51	19.5-21.9	5.39 (100 kPa)	thermodynamic	[28]
	CPM-231 [14]	powder	298	6.77	-	18.3-24.4	-	thermodynamic	[29]
	PCN-222 [15]	powder	298	1.16	4.51	18.3	4.7 (100 kPa) 3.37 (500 kPa)	thermodynamic	[30]
	UTSA-120 [16]	powder	296	5.04	5.25	27-31	95.4 (100 kPa)	thermodynamic	[31]
	SIFSIX-2-Cu-i [16]			5.44	7.35	-	29.7 (100 kPa)		
	ZU-301 [17]	powder	298	2.41	2.45	37-41	92.8 (100 kPa) 108 (500 kPa)	thermodynamic	[32]
	MOF-808@N [18]	powder	298	1.31	3.60	16.9-29.1	7.80 (100 kPa) 8.50 (500 kPa)	thermodynamic	[33]
	MOF-808 [18]			1.22	3.77	18.0-32.4	8.56 (100 kPa) 8.21 (500 kPa)		
	DUT-67@N [18]			1.29	3.71	25.0-29.0	6.47 (100 kPa) 5.53 (500 kPa)		
	DUT-67 [18]			1.24	3.72	31.7-41.0	5.72 (100 kPa) 5.41 (500 kPa)		
	MIL-53(Al) [19]	powder	298	2.64	3.34	23.3	14.3 (100 kPa)	thermodynamic	[34]
		beads		2.16	3.09	21.5	11.3 (100 kPa)		
	MIL-101(Cr) [19]	powder		1.49	4.60	26.2	4.08 (100 kPa)		
		beads		1.08	3.05	22.6	3.70 (100 kPa)		

Table S10 (*cont.*). Benchmarking of the CO_2/CH_4 separation performance of MFU-4 against literature-reported adsorbent materials.

Type	Material	Form	T. (K)	q_{CO_2} (mol/kg)		Q_{st,CO_2} (kJ/mol)	S_{CO_2/CH_4} (-)	Separation Mechanism CO_2/CH_4	Reference
				100 kPa	500 kPa				
MOF	TAMOF-1 [20]	powder	298	4.03	6.07	27.9-44.4	(i) 32.8 (100 kPa) (i) 36.1 (500 kPa) (ii) 6 (100 kPa)	thermodynamic	[35]
	MIL-160(Al) [21]	powder	298	3.89	5.79	33	(i) 8.37 (100 kPa) (i) 10.1 (500 kPa)	thermodynamic	[36,37]
		beads		2.81	4.42	-	(i) 9.73 (100 kPa) (i) 10.5 (500 kPa) (ii) 18.4 (115 kPa)		
	IITKGP-21a [22]	powder	295	1.86	3.14	22	4.4 (100 kPa)	thermodynamic	[38]
	MIL-120(Al) [23]	powder	298	3.56	4.59	36.7-43.1	(i) 22.2 (100 kPa) (i) 30.6 (500 kPa)	thermodynamic	[39]
		beads		3.33	4.28	-	(i) 24.9 (100 kPa) (i) 30.7 (500 kPa) (ii) 89.3 (100 kPa)		
	MFU-4 [24]	**powder**	**298**	**3.61**	**7.36**	**24.4**	**66.8**	**kinetic**	**this work**
PILC	$(Al_2O_3)_B$ [25]	powder	298	0.36	0.90	-	9.19 (100 kPa)	thermodynamic	[40]
	$(Al_2O_3)_W$ [25]			0.42	1.10		12.5 (100 kPa)		
	$(ZrO_2)_B$ [25]			0.27	0.88		5.15 (100 kPa)		
	$(ZrO_2)_W$ [25]			0.41	0.91		34.6 (100 kPa)		
PMO	Ph-PMO [26]	powder	298	0.37	1.31	-	4.26 (100 kPa) 5.58 (500 kPa)	thermodynamic	[41]
	NH_2-Ph-PMO [26]			0.40	1.50		4.26 (100 kPa) 5.40 (500 kPa)		
	APTMS@Ph-PMO [26]			0.71	1.72		9.74 (100 kPa) 11.5 (500 kPa)		
	APTMS@NH_2-Ph-PMO [26]			0.50	1.22		8.85 (100 kPa) 12.0 (500 kPa)		

Table S10 (*cont.*). Benchmarking of the CO_2/CH_4 separation performance of MFU-4 against literature-reported adsorbent materials.

Type	Material	Form	T. (K)	q_{CO_2} (mol/kg)		Q_{st,CO_2} (kJ/mol)	S_{CO_2/CH_4} (-)	Separation Mechanism CO_2/CH_4	Reference
				100 kPa	500 kPa				
Silica	MCM-41 [27]	powder	298	0.68	2.74	18.9-21.2	5.15 (100 kPa) 5.12 (500 kPa)	thermodynamic	[42,43]
	SBA-15 [28]			0.64	1.95		6.52 (100 kPa) 8.53 (500 kPa)		
	N-3@SBA-15 [28]	powder	298	1.39	1.86	-	15577 (100 kPa) 14421 (500 kPa)	thermodynamic	[44]
	TMMAP@SBA-15 [28]			1.03	1.49		396 (100 kPa) 1096 (500 kPa)		
	APTES@SBA-15 [29]	powder	298	0.57	1.33	-	12.1 (100 kPa) 9.74 (500 kPa)	thermodynamic	[45]
	DEAPTES@SBA-15 [29]			0.34	0.88		5.80 (100 kPa) 4.96 (500 kPa)		
Zeolite	13X [30]	pellets granules	298	4.58	5.89	37.2	88 (100 kPa) 66 (500 kPa)	thermodynamic	[27,46]
	NaX [31]	n.s.	303	4.82	5.80	38-49	-	thermodynamic	[26]
	Silicalite-1 [32]			1.69	2.59	26.1-29.9	2.9 (100 kPa)		
	DDR [32]	powder	298	1.37	2.17	28.2-42.0	4.6 (100 kPa)	thermodynamic	[47]
	BETA [32]			2.05	3.22	18.6-58.2	4.6 (100 kPa)		
	5A [33]	beads	303	3.06	3.61	23.2-45.6	-	thermodynamic	[48]
	4A [34]	powder	298	4.29	4.99	36.2+1.6 42.9	-	thermodynamic	[49]
	Na-ZSM-5 [35]	pellets	293	1.39	2.24	26.5-29.5	-	thermodynamic	[50]
	Sr-ETS-4 [36]	powder	293	1.08	1.77	-	26.6	kinetic	[14–16]
	Ba-ETS-4 [36]			1.48	2.08	-	35.5		

Table S10 (*cont.*). Benchmarking of the CO_2/CH_4 separation performance of MFU-4 against literature-reported adsorbent materials.

Type	Material	Form	T. (K)	q_{CO_2} (mol/kg)		Q_{st,CO_2} (kJ/mol)	S_{CO_2/CH_4}	Separation Mechanism CO_2/CH_4	Reference
				100 kPa	500 kPa				
Zeolite	NaY [37]	powder	298	5.44	6.54	29.6-37.9	65.7 (100 kPa) 55.8 (500 kPa)	thermodynamic	[51]
	0.5%PEPO-NaY [37]			4.10	5.01	28.4-35.8	70.8 (100 kPa) 95.3 (500 kPa)		
	1%PEPO-NaY [37]			3.20	4.00	27.9-34.0	45.8 (100 kPa) 70.7 (500 kPa)		
	2%PEPO-NaY [37]			2.21	2.81	27.1-34.0	38.3 (100 kPa) 56.1 (500 kPa)		

Notes from Table S10:

n.s. – not specified

[1] q_{CO_2} (from Sips model fitting) calculated using parameters provided in Table 6; Q_{st,CO_2} (from Clausius-Clapeyron equation) range obtained from Figure 6.

[2] q_{CO_2} (from Toth model fitting) calculated using parameters provided in Table 6; Q_{st,CO_2} (from Clausius-Clapeyron equation) range obtained from Figure 3; S_{CO_2/CH_4}(from IAST for CO_2:CH_4=50:50 vol.%) value obtained from Figure 4.

[3] q_{CO_2} (from isotherm) value obtained from Figure 3; S_{CO_2/CH_4} (from uptakes of a CO_2:CH_4=50:50 vol.% breakthrough experiment), calculated from values reported in Table 3.

[4] q_{CO_2} (from isotherm) value obtained from Figure 1; Q_{st,CO_2} (from Clausius-Clapeyron equation) average value reported in the main text; S_{CO_2/CH_4} (from uptakes of a CO_2:CH_4=50:50 vol.% breakthrough experiment) value reported in Table 2.

[5] q_{CO_2} (from DSL model fitting) calculated using parameters provided in Table 5; S_{CO_2/CH_4} (from Hobgood formulation, Eq. S10 of this work) calculated using the intracrystalline diffusivities of CO_2 and CH_4 reported in Table S9 of this work.

[6] q_{CO_2} (from Multisite Langmuir model fitting) calculated using parameters provided in Table 3.4; S_{CO_2/CH_4} (from Hobgood formulation, Eq. S10 of this work) calculated using the intracrystalline diffusivities of CO_2 and CH_4 reported in Table 3.6.

[7] q_{CO_2} (from Sips model fitting) calculated using parameters provided in Table 3; S_{CO_2/CH_4} (from Hobgood formulation, Eq. S10 of this work) calculated using the intracrystalline diffusivities of CO_2 and CH_4 reported in Table 3.

[8] q_{CO_2} (from Dual-Site Sips model fitting) calculated using parameters provided in Table 3 (extrapolated to 500 kPa); Q_{st,CO_2} (from Clausius-Clapeyron equation) range obtained from Figure 8;

[9] q_{CO_2} (from DSL model fitting) calculated using parameters provided in Table S13 (extrapolated to 500 kPa); Q_{st,CO_2} (from Clausius-Clapeyron equation) constant value obtained from Figure 2a; S_{CO_2/CH_4}(from IAST for CO_2:CH_4=50:50 vol.%) value obtained from Figure 2c.

[10] q_{CO_2} (from Triple-Site Langmuir (TSL) model fitting) calculated using parameters provided in Table S2; S_{CO_2/CH_4}(from IAST for CO_2:CH_4=50:50 vol.%) value reported in Table 2.

[11] q_{CO_2} (from Toth model fitting) calculated using parameters provided in Table S2; Q_{st,CO_2} (from microcalorimetry experiments at 303 K) range/value reported in Table 4.

[12] q_{CO_2} (from isotherm) value obtained from Figure 1a; Q_{st,CO_2} (from Clausius-Clapeyron equation) value reported in the main text; S_{CO_2/CH_4} (from uptakes of a CO_2:CH_4=60:40 vol.% breakthrough experiment) value reported in Table 3.

[13] q_{CO_2} (from Dual-Site Sips model fitting) calculated using parameters provided in Table S3 (extrapolated to 500 kPa); Q_{st,CO_2} (from Clausius-Clapeyron equation) range obtained from Figure S8b; S_{CO_2/CH_4}(from IAST for CO_2:CH_4=50:50 vol.%) value obtained from Figure 5b.

[14] q_{CO_2} reported in the main text; Q_{st,CO_2} (from Clausius-Clapeyron equation) range obtained from Figure S55.

[15] q_{CO_2} (from Dual-Site Sips model fitting) calculated using parameters provided in Tables S2-S3; Q_{st,CO_2} (from Clausius-Clapeyron equation) value reported in Table 1; S_{CO_2/CH_4}(from IAST for CO_2:CH_4=50:50 vol.%) value obtained from Figures 6a-7a.

[16] q_{CO_2} (from Dual-Site Sips model fitting) calculated using parameters provided in Table S2; Q_{st,CO_2} (from Clausius-Clapeyron equation) range reported in the main text; S_{CO_2/CH_4}(from IAST for CO_2:CH_4=50:50 vol.%) value obtained from Figure S12.

[17] q_{CO_2} (from Sips model fitting) calculated using parameters provided in Table S4; Q_{st,CO_2} (from Clausius-Clapeyron equation) range reported in the main text; S_{CO_2/CH_4}(from IAST for CO_2:CH_4=50:50 vol.%) value obtained from Figure 2b.

[18] q_{CO_2} (from isotherms) values obtained from Figures 9a-10a; Q_{st,CO_2} (from Clausius-Clapeyron equation) range obtained from Figure 12; S_{CO_2/CH_4}(from IAST for CO_2:CH_4=50:50 vol.%) value obtained from Figure 11b-d.

[19] q_{CO_2} (from DSL model fitting) calculated using parameters provided in Table S2 (extrapolated to 500 kPa); Q_{st,CO_2} (from Clausius-Clapeyron equation) value reported in Table 2; S_{CO_2/CH_4}(from IAST for CO_2:CH_4=50:50 vol.%) value reported in the main text.

[20] q_{CO_2} (from isotherm) value obtained from Figure 2a; Q_{st,CO_2} (from Clausius-Clapeyron equation) range obtained from Figure S13; S_{CO_2/CH_4} (i) (from IAST for CO_2:CH_4=50:50 vol.%) value reported in Table S18 and (ii) (from uptakes of a CO_2:CH_4=50:50 vol.% breakthrough experiment) value reported in Table S19.

[21] q_{CO_2} (from Virial model fitting) calculated using parameters provided in Table S16 (beads with d_p 1-1.4 mm);[36] Q_{st,CO_2} (from Clausius-Clapeyron equation) value reported for low coverage in the main text;[37] S_{CO_2/CH_4} (i) (from IAST as the mean selectivity) value obtained from Figure S9 and (ii) (from uptakes of a CO_2:CH_4=50:50 vol.% breakthrough experiment) calculated from values reported in Table 4.[36]

[22] q_{CO_2} (from Langmuir model fitting) calculated using parameters provided in Table S5 (extrapolated to 500 kPa); Q_{st,CO_2} (from Clausius-Clapeyron equation) constant value obtained from Figure S8; S_{CO_2/CH_4}(from IAST for CO_2:CH_4=50:50 vol.%) value reported in the main text.

[23] q_{CO_2} (from Virial model fitting) calculated using parameters provided in Table S3; Q_{st,CO_2} (from Clausius-Clapeyron equation) range obtained from Figure 2c; S_{CO_2/CH_4}(i) (from IAST as the mean selectivity) value obtained from Figure S5 and (ii) (from uptakes of a CO_2:CH_4=50:50 vol.% breakthrough experiment) calculated from values reported in Table S9.

[24] q_{CO_2} (from uptake of a single-component breakthrough experiment) value reported in Table S4; Q_{st,CO_2} (from Clausius-Clapeyron equation) constant value represented in Figure S12; S_{CO_2/CH_4} (from Hobgood formulation, Eq. S10) calculated using the intracrystalline diffusivities of CO_2 and CH_4 reported in Table S9.

[25] q_{CO_2} (from Virial model fitting) calculated using parameters provided in Table S2; S_{CO_2/CH_4}(from IAST for CO_2:CH_4=50:50 vol.%) value obtained from Figure 4.

[26] q_{CO_2} (from Virial model fitting) calculated using parameters provided in Table 1; S_{CO_2/CH_4}(from IAST as the mean selectivity) value obtained from Figure 5.

[27] q_{CO_2} (from Toth model fitting) calculated using parameters provided in Table 1;[42] Q_{st,CO_2} (from Clausius-Clapeyron equation) range obtained from Figure 11;[43] S_{CO_2/CH_4}(from IAST for CO_2:CH_4=50:50 vol.%) value obtained from Figure 6.[42]

[28] q_{CO_2} (from Virial model fitting) calculated using parameters provided in Table 2; S_{CO_2/CH_4}(from IAST as the mean selectivity) value obtained from Figure 4.

[29] q_{CO_2} (from Langmuir-Virial model fitting) calculated using parameters provided in Table 2; S_{CO_2/CH_4}(from IAST as the mean selectivity) value obtained from Figures 3-4.

[30] Material used as pellets[46] and granules;[27] q_{CO_2} (from Multisite Langmuir model fitting) calculated using parameters provided in Table 6;[46] Q_{st,CO_2} value reported for low-pressure data (linear range of the isotherm) in the main text;[46] S_{CO_2/CH_4} (from uptakes of a CO_2:CH_4=60:40 vol.% breakthrough experiment) value reported in Table 3.[27]

[31] q_{CO_2} (from Toth model fitting) calculated using parameters provided in Table S2; Q_{st,CO_2} (from microcalorimetry experiments at 303 K) range/value reported in Table 4.

[32] q_{CO_2} (from Langmuir model fitting) calculated using parameters in Table S1 (molar volume STP: 22711 cm^3/mol); Q_{st,CO_2} (from Clausius-Clapeyron equation) range obtained from Figure 8; S_{CO_2/CH_4}(from IAST for CO_2:CH_4=50:50 vol.%) value obtained from Figure 6.

[33] q_{CO_2} (from Sips model fitting) calculated using parameters provided in Table 2; Q_{st,CO_2} (from Clausius-Clapeyron equation) range obtained from Figure 4.

[34] q_{CO_2} provided in Online resource 6; Q_{st,CO_2} values reported in Table 2.

[35] q_{CO_2} (from Toth model fitting) calculated using parameters provided in Table 5; Q_{st,CO_2} (from Clausius-Clapeyron equation) range obtained from Figure 9.

[36] q_{CO_2} (from Sips model fitting) calculated using parameters provided in Table S1 (n estimated as it was not reported); [16] S_{CO_2/CH_4} (from Hobgood formulation, Eq. S10 of this work) calculated using the intracrystalline diffusivities of CO_2 and CH_4 reported in Table S9 of this work.[14–16]

[37] q_{CO_2} (from isotherm) value obtained from Figure 6; Q_{st,CO_2} range obtained from Figure S4; S_{CO_2/CH_4} (from IAST for CO_2:CH_4=50:50 vol.%) value reported in Table 3.

References

[1] Q. Liu, S. G. Cho, J. Hilliard, T. Y. Wang, S. C. Chien, L. C. Lin, A. C. Co, C. R. Wade, "Inverse CO_2/C_2H_2 separation with MFU-4 and selectivity reversal via postsynthetic ligand exchange" *Angew. Chem. Int. Ed.* **2023**, *62*, e202218854.

[2] L. Zhou, P. Brântuas, A. Henrique, H. Reinsch, M. Wahiduzzaman, J. M. Grenèche, A. E. Rodrigues, J. A. C. Silva, G. Maurin, C. Serre, "A Microporous Multi-Cage Metal–Organic Framework for an Effective One-Step Separation of Branched Alkanes Feeds" *Angew. Chem. Int. Ed.* **2024**, *63*, e202320008.

[3] D. D. Do, *Adsorption Analysis: Equilibria and Kinetics*, Imperial College Press, **1998**.

[4] D. M. Ruthven, *Principles of Adsorption and Adsorption Processes*, John Wiley & Sons, **1984**.

[5] A. Nuhnen, C. Janiak, "A practical guide to calculate the isosteric heat/enthalpy of adsorption: Via adsorption isotherms in metal-organic frameworks, MOFs" *Dalton Transactions* **2020**, *49*, 10295–10307.

[6] S. Sircar, J. R. Hufton, "Why does the linear driving force model for adsorption kinetics work?" *Adsorption* **2000**, *6*, 137–147.

[7] Aspentech, *Aspen AdsimTM 11.1 - Adsorption Reference Guide*, Cambridge, **2001**.

[8] D. F. Fairbanks, C. R. Wilke, "Diffusion coefficients in multicomponent gas mixtures" *Ind. Eng. Chem.* **1950**, *42*, 471–475.

[9] B. E. Poling, J. M. Prausnitz, J. P. O´Connell, *The Properties of Gases and Liquids*, McGraw-Hill, **2001**.

[10] H. W. Habgood, "The Kinetics of Molecular Sieve Action. Sorption of Nitrogen- Methane Mixtures by Linde Molecular Sieve 4A" *Can. J. Chem.* **1958**, *36*, 1384–1397.

[11] S. Cavenati, Separação de Misturas $CH_4/CO_2/N_2$ Por Processos Adsorptivos, Faculdade de Engenharia da Universidade do Porto, **2005**.

[12] K. Y. Foo, B. H. Hameed, "Insights into the modeling of adsorption isotherm systems" *Chemical Engineering Journal* **2010**, *156*, 2–10.

[13] G. Sastre, J. Van Den Bergh, F. Kapteijn, D. Denysenko, D. Volkmer, "Unveiling the mechanism of selective gate-driven diffusion of CO2 over N2 in MFU-4 metal-organic framework" *Dalton Transactions* **2014**, *43*, 9612–9619.

[14] R. P. Marathe, S. Farooq, M. P. Srinivasan, "Modeling gas adsorption and transport in small-pore titanium silicates" *Langmuir* **2005**, *21*, 4532–4546.

[15] B. Majumdar, S. J. Bhadra, R. P. Marathe, S. Farooq, "Adsorption and diffusion of methane and nitrogen in barium exchanged ETS-4" *Ind. Eng. Chem. Res.* **2011**, *50*, 3021–3034.

[16] Q. Peng, Y. Chen, D. Fang, C. Liu, K. Wu, Y. Chen, H. Jiang, Y. Sun, Q. Wu, D. Wu, H. Sun, "Enhancing size-selective adsorption of CO_2/CH_4 on ETS-4 via ion-exchange coupled with thermal treatment" *Ind. Eng. Chem. Res.* **2023**, *62*, 9313–9324.

[17] C. A. Grande, R. Blom, A. Möller, J. Möllmer, "High-pressure separation of CH_4/CO_2 using activated carbon" *Chem. Eng. Sci.* **2013**, *89*, 10–20.

[18] N. Álvarez-Gutiérrez, M. V. Gil, F. Rubiera, C. Pevida, "Adsorption performance indicators for the CO_2/CH_4 separation: Application to biomass-based activated carbons" *Fuel Processing Technology* **2016**, *142*, 361–369.

[19] N. Álvarez-Gutiérrez, S. García, M. V. Gil, F. Rubiera, C. Pevida, "Dynamic performance of biomass-based carbons for CO2/CH4 separation. Approximation to a pressure swing adsorption process for biogas upgrading" *Energy and Fuels* **2016**, *30*, 5005–5015.

[20] I. Durán, N. Álvarez-Gutiérrez, F. Rubiera, C. Pevida, "Biogas purification by means of adsorption on pine sawdust-based activated carbon: Impact of water vapor" *Chemical Engineering Journal* **2018**, *353*, 197–207.

[21] L. A. M. Rocha, K. A. Andreassen, C. A. Grande, "Separation of CO_2/CH_4 using carbon molecular sieve (CMS) at low and high pressure" *Chem. Eng. Sci.* **2017**, *164*, 148–157.

[22] M. Azadi Tabar, E. Pancione, S. A. Peter, J. F. M. Denayer, "Four-column vacuum pressure swing adsorption for biogas upgrading with co-production of high-purity biogenic CO_2: experimental and simulation study" *Journal of CO2 Utilization* **2026**, *105*, 103348.

[23] Z. Bao, L. Yu, Q. Ren, X. Lu, S. Deng, "Adsorption of CO_2 and CH_4 on a magnesium-based metal organic framework" *J. Colloid Interface Sci.* **2011**, *353*, 549–556.

[24] S. Xiang, Y. He, Z. Zhang, H. Wu, W. Zhou, R. Krishna, B. Chen, "Microporous metal-organic framework with potential for carbon dioxide capture at ambient conditions" *Nat. Commun.* **2012**, *3*.

[25] A. D. Wiersum, C. Giovannangeli, D. Vincent, E. Bloch, H. Reinsch, N. Stock, J. S. Lee, J. S. Chang, P. L. Llewellyn, "Experimental screening of porous materials for high pressure gas adsorption and evaluation in gas separations: application to MOFs (MIL-100 and CAU-10)" *ACS Comb. Sci.* **2013**, *15*, 111–119.

[26] A. D. Wiersum, J. S. Chang, C. Serre, P. L. Llewellyn, "An adsorbent performance indicator as a first step evaluation of novel sorbents for gas separations: application to metal-organic frameworks" *Langmuir* **2013**, *29*, 3301–3309.

[27] S. A. Peter, G. V. Baron, J. Gascon, F. Kapteijn, J. F. M. Denayer, "Dynamic desorption of CO_2 and CH_4 from amino-MIL-53(Al) adsorbent" *Adsorption* **2013**, *19*, 1235–1244.

[28] J. Cai, H. Wang, H. Wang, X. Duan, Z. Wang, Y. Cui, Y. Yang, B. Chen, G. Qian, "An amino-decorated NbO-type metal-organic framework for high C2H2 storage and selective CO_2 capture" *RSC Adv.* **2015**, *5*, 77417–77422.

[29] Q. G. Zhai, X. Bu, C. Mao, X. Zhao, L. Daemen, Y. Cheng, A. J. Ramirez-Cuesta, P. Feng, "An ultra-tunable platform for molecular engineering of high-performance crystalline porous materials" *Nat. Commun.* **2016**, *7*, 13645.

[30] D. Lv, R. Shi, Y. Chen, Y. Chen, H. Wu, X. Zhou, H. Xi, Z. Li, Q. Xia, "Selective adsorptive separation of CO_2/CH_4 and CO_2/N_2 by a water resistant zirconium-porphyrin metal-organic framework" *Ind. Eng. Chem. Res.* **2018**, *57*, 12215–12224.

[31] H. M. Wen, C. Liao, L. Li, A. Alsalme, Z. Alothman, R. Krishna, H. Wu, W. Zhou, J. Hu, B. Chen, "A metal-organic framework with suitable pore size and dual functionalities for highly efficient post-combustion CO_2 capture" *J. Mater. Chem. A Mater.* **2019**, *7*, 3128–3134.

[32] C. Yu, Q. Ding, J. Hu, Q. Wang, X. Cui, H. Xing, "Selective capture of carbon dioxide from humid gases over a wide temperature range using a robust metal–organic framework" *Chemical Engineering Journal* **2021**, *405*, 126937.

[33] H. N. Wamba, S. Dalakoti, N. Singh, S. Divekar, J. Ngoune, A. Arya, S. Dasgupta, "Facile aqueous medium synthesis of highly stable Zr-MOFs with promising CO_2/CH_4 adsorption selectivity for natural gas and biogas upgradation" *Ind. Eng. Chem. Res.* **2023**, *62*, 19773–19783.

[34] N. Singh, S. Dalakoti, A. Sharma, R. Chauhan, R. S. Murali, S. Divekar, S. Dasgupta, Aarti, "Shaping of MIL-53-Al and MIL-101 MOF for CO_2/CH_4, CO_2/N_2 and CH_4/N_2 separation" *Sep. Purif. Technol.* **2024**, *341*.

[35] S. Capelo-Avilés, M. de Fez-Febré, S. R. G. Balestra, J. Cabezas-Giménez, R. Tomazini de Oliveira, I. I. Gallo Stampino, A. Vidal-Ferran, J. González-Cobos, V. Lillo, O. Fabelo, E. C. Escudero-Adán, L. R. Falvello, J. B. Parra, P. Rumori, G. Turnes Palomino, C. Palomino Cabello, S. Giancola, S. Calero, J. R. Galán-Mascarós, "Selective adsorption of CO_2 in TAMOF-1 for the separation of CO2/CH4 gas mixtures" *Nature Communications* **2025**, *16*, 3243.

[36] M. Bordonhos, M. I. S. Neves, A. Marandi, F. Nouar, M. Jorge, J. R. B. Gomes, C. Serre, M. L. Pinto, "Spanning the molecular to industrial scale of the adsorption-based separation of CO_2/CH_4 by MIL-160(Al)" *Chemical Engineering Journal* **2025**, *524*, 169276.

[37] D. Damasceno Borges, P. Normand, A. Permiakova, R. Babarao, N. Heymans, D. S. Galvao, C. Serre, G. De Weireld, G. Maurin, "Gas Adsorption and Separation by the Al-Based Metal-Organic Framework MIL-160" *Journal of Physical Chemistry C* **2017**, *121*, 26822–26832.

[38] R. Sahoo, B. Pramanik, R. Krishna, M. C. Das, "A chemically robust 3D interpenetrated MOF toward one-step methane purification along with six other multipurpose gas separations" *Small* **2026**, *22*, e72629.

[39] M. Bordonhos, R. V. Pinto, T. Frade, B. Chen, F. Nouar, G. Mouchaham, J. R. B. Gomes, C. Serre, M. L. Pinto, "Towards sustainable biogas upgrading: MIL-120(Al) as a cost-effective water stable MOF for CO2/CH4 separation" *J. Mater. Chem. A Mater.* **2026**, *14*, 12856–12866.

[40] J. Pires, V. K. Saini, M. L. Pinto, "Studies on selective adsorption of biogas components on pillared clays: Approach for biogas improvement" *Environ. Sci. Technol.* **2008**, *42*, 8727–8732.

[41] M. A. O. Lourenço, C. Siquet, M. Sardo, L. Mafra, J. Pires, M. Jorge, M. L. Pinto, P. Ferreira, J. R. B. Gomes, "Interaction of CO_2 and CH_4 with functionalized periodic mesoporous phenylene-silica: periodic DFT calculations and gas adsorption measurements" *Journal of Physical Chemistry C* **2016**, *120*, 3863–3875.

[42] Y. Belmabkhout, A. Sayari, "Adsorption of CO2 from dry gases on MCM-41 silica at ambient temperature and high pressure. 2: Adsorption of CO_2/N_2, CO_2/CH_4 and CO_2/H_2 binary mixtures" *Chem. Eng. Sci.* **2009**, *64*, 3729–3735.

[43] Y. Belmabkhout, R. Serna-Guerrero, A. Sayari, "Adsorption of CO_2 from dry gases on MCM-41 silica at ambient temperature and high pressure. 1: Pure CO_2 adsorption" *Chem. Eng. Sci.* **2009**, *64*, 3721–3728.

[44] L. Mafra, T. Čendak, S. Schneider, P. V. Wiper, J. Pires, J. R. B. Gomes, M. L. Pinto, "Amine functionalized porous silica for CO_2/CH_4 separation by adsorption: Which amine and why" *Chemical Engineering Journal* **2018**, *336*, 612–621.

[45] M. Pacheco, M. Bordonhos, M. Sardo, R. Afonso, J. R. B. Gomes, L. Mafra, M. L. Pinto, "Moisture effect on the separation of CO_2/CH_4 mixtures with amine-functionalised porous silicas" *Chemical Engineering Journal* **2022**, *443*, 136271.

[46] S. Cavenati, C. A. Grande, A. E. Rodrigues, "Adsorption Equilibrium of methane, carbon dioxide, and nitrogen on zeolite 13X at high pressures" *J. Chem. Eng. Data* **2004**, *49*, 1095–1101.

[47] J. Yang, J. Li, W. Wang, L. Li, J. Li, "Adsorption of CO_2, CH_4, and N_2 on 8-, 10-, and 12-membered ring hydrophobic microporous high-silica zeolites: DDR, Silicalite-1, and Beta" *Ind. Eng. Chem. Res.* **2013**, *52*, 17856–17864.

[48] M. Mofarahi, F. Gholipour, "Gas adsorption separation of CO_2/CH_4 system using zeolite 5A" *Microporous and Mesoporous Materials* **2014**, *200*, 1–10.

[49] K. G. Wynnyk, B. Hojjati, P. Pirzadeh, R. A. Marriott, "High-pressure sour gas adsorption on zeolite 4A" *Adsorption* **2017**, *23*, 149–162.

[50] M. Rahmani, B. Mokhtarani, M. Mafi, N. Rahmanian, "Acid gas removal by superhigh silica ZSM-5: adsorption isotherms of hydrogen sulfide, carbon dioxide, methane, and nitrogen" *Ind. Eng. Chem. Res.* **2022**, *61*, 6600–6610.

[51] A. Sharma, A. Verma, U. Kumar, N. Singh, S. Dalakoti, R. Chauhan, S. Bhandari, S. Divekar, S. Dasgupta, Aarti, "Interchangeable effect of polyols-based zeolite on the separation of CO_2, CH_4, and N_2 gases" *Microporous and Mesoporous Materials* **2024**, *367*, 112984.